NBS-GCR-81-304

An Investigation of Fire Impingement on A Horizontal Ceiling

December 1981

Sponsored by
U.S. DEPARTMENT OF COMMERCE
National Bureau of Standards
Center for Fire Research
Washington, DC 20234

AN INVESTIGATION OF FIRE IMPINGEMENT ON A HORIZONTAL CEILING

Summary

This report discusses research completed under NBS Grant No. 7-9020, during the period September 1, 1979 to August 31, 1980. The structure and heat transfer properties of fires and fire plumes impinging on a horizontal ceiling were investigated.

The experiments employed an apparatus with a water-cooled ceiling, 1000 mm in diameter, located 400 mm above the fire source. The fire source was simulated by a natural gas fueled burner, having a diameter of 55 mm. A number of burner operating conditions were studied; however, the experiments emphasized two flame conditions with energy rates of 1.67 and 8.51 kW, respectively. The luminous tip of the smaller flame just impinged on the ceiling, while the larger flame spread roughly half-way across the ceiling. Source Reynolds numbers were less than 400 for both flames; therefore, buoyancy effects dominated the flows.

Profiles of mean velocity, temperature, composition and mixture fraction were measured. Turbulence quantities were also measured in the plume, including longitudinal fluctuations and Reynolds stress. Other measurements were as follows: convective and radiative heat fluxes to the ceiling, radiative heat flux to the surroundings, and flame shape. In addition to reporting the profile measurements directly, the results were reduced to yield average properties (velocity, temperature, composition and width) corresponding to "top hat" profiles.

The measurements were compared with predictions of both differential and integral models. A k-ε-g differential model was examined for the plume portion of the flow. This model was originally developed for forced combusting flows and while it includes buoyancy effects in the mean equations, the effect of buoyancy on turbulence quantities is ignored. The prediction of radiation was simplified, in order to avoid complications due to the presence of soot, by either neglecting radiative heat losses entirely or by assuming that a fixed fraction, 20%, of the energy released by combustion was lost due to radiation.

Integral models were developed for both the plume and ceiling jet portions of the flow. Computational convenience was emphasized during the construction of these models; therefore, "top hat" profiles a flow entrainment expression, and a mixing-controlled combustion model are assumed.

A summary of the findings of the investigation follows:

Plume:

Differential Model. The k-ε-g model provided a reasonable indication of the trends of the flow; however, errors between predictions and measurements were greater than those found for forced combusting flows using the same model.

The greatest discrepancy between predictions and measurements involved the width of the flow, which the theory underestimated by as much as 50% in the upper portion of the flames. Room disturbances, resulting in a nonturbulent deflection of the flow, are felt to be mainly responsible for this discrepancy. Low Reynolds number effects, the influence of buoyancy on turbulence properties, uncertainties in estimating initial conditions, and experimental uncertainties are also factors contributing to errors in predictions.

Allowing for radiative heat losses yielded some improvement of the predictions; however, the effect was not large. Use of two different sets of model constants, each set currently advocated by others, did not have a significant impact on the overall comparison between predictions and measurements.

Integral Model. The present integral model provided fair agreement between predictions and measurements for both weakly buoyant plumes and flames; however, optimum performance of the model for these cases was observed for slightly different values of the entrainment constants. The data base for these comparisons included the present measurements, and results obtained by McCaffrey, Cox and Chitty, and Zukoski and coworkers, among others.

These results indicate that incorporating a Rayleigh number dependence in the entrainment coefficient expression would probably provide a more universal modeling procedure, valid for both weakly buoyant plumes and natural fires. Work is in progress in this laboratory to complete this extension.

The integral model provided good results for average velocity, temperature and composition in both combusting and noncombusting plumes. Estimations of radiative heat fluxes, however, were less satisfactory. This behavior is due to the use of average quantities, i.e., assuming "top hat" profiles. Since radiation is a nonlinear function of temperature, such averaging results in an underestimation of radiation levels. The use of profiles providing a more realistic approximation of flame structure would be required to eliminate this defect, although this would complicate the model appreciably.

Ceiling Jet:

The present integral model provided a reasonable prediction of both flow properties and ceiling heat fluxes. The evaluation of the model included measurements reported by Alpert, Zukoski and coworkers,

and the present investigation; therefore, both combusting and non-combusting ceiling jets were considered. The estimation of flow properties was greatly influenced by entrainment characteristics. Ceiling friction, on the other hand, had only a secondary effect on structure predictions. The computations showed that the parameters $qH^2/\dot{Q}$ and r/H cannot completely correlate ceiling heat fluxes for a wide range of heat sources. However, the parameter $(qH^2/\dot{Q})Ra^{1/6}$, suggested during an earlier phase of this investigation, provides a good correlation of the ceiling heat flux measurements.

Acknowledgement

This research was supported by the United States Department of Commerce, National Bureau of Standards, Grant No. 7-9020. Dr. Howard Baum of the Center for Fire Research was the NBS Scientific Officer for the project.

Table of Contents

	Page
Summary	ii
Acknowledgement	v
List of Tables	vii
List of Figures	viii
Nomenclature	x
1. Introduction	1
2. Experimental Methods	2
2.1 Apparatus	2
2.2 Instrumentation	5
3. Theory -- Plume Region	7
3.1 Differential Model	7
3.1.1 Description of Model	7
3.1.2 Equation of State	8
3.1.3 Governing Equations	8
3.1.4 Computations	11
3.2 Integral Model	14
3.2.1 Description of Model	14
3.2.2 Governing Equations	15
3.2.3 Computations	16
4. Results and Discussion--Plume Region	19
4.1 Test Conditions	19
4.2 Comparison of Differential Model Predictions and Measurements	21
4.3 Comparison of Integral Model Predictions and Measurements	36
5. Theory--Ceiling Jet Region	48
5.1 Description of Model	48
5.2 Governing Equations	48
5.3 Parameters in the Governing Equations	50
5.4 Computations	51
6. Results and Discussion--Ceiling Jet Region	52
6.1 Predicted and Measured Flow Structure	52
6.2 Predicted and Measured Heat Transfer Rates	58
6.3 Effect of Radiation on Heat Flux	61
References	64

List of Tables

Table		Page
1	Composition of Fuel Gas.	4
2	Constants in the Turbulence Model.	12
3	Summary of Natural Gas Diffusion Flames.	20
4	Mass Conservation Balances of Flame I and Flame II . .	22
5	Constants for the Integral Model	42

Nomenclature

Symbol	Description
A_i	Quantities defined in Equations (3.22)-(3.25)
a	Gravitational acceleration
B_i	Quantities defined in Equations (5.5)-(5.8)
C_c	Entrainment constant defined in Equation (5.13)
C_i	Constants in Equation (3.40) where i = 1 and 2
C_j	Constants used in turbulence model
C_p	Specific heat of gas mixture
C_{p_i}	Specific heat of species i
C_r	Reaction rate constant
D	Source diameter
D_k	Characteristic band width
f	Mixture fraction; ceiling skin friction
g	Square of mixture fraction fluctuations
H	Ceiling height
H_f	Flame height
H_R	Flame length along the ceiling
h	Ceiling thickness for top hat profile
h_c	Ceiling heat transfer coefficient
$h_i^{(o)}$	Standard heat of formation of species i
$I_{b,k}$	Blackbody spectral intensity
K	Constant in Equation (3.14)
k	Kinetic energy of turbulence; thermal conductivity of gas mixture
ℓ_m	Mixing length
$\dot{m}$	Mass flow rate

Symbol	Description
P_i	Production rate of species i
$P(f)$	Probability density function
Pr	Prandtl number
$\dot{Q}$	Thermal energy flux of plumes
Q_R	Radiation loss per unit volume
Q_c	Heat of combustion
q	Heat flux per unit area
Ra	Rayleigh number
Ri	Richardson number
r	Radial coordinate of plumes and ceiling jets
r_f	Stoichiometry parameter, mass of air to mass of fuel
Sg_k	Surface-gas exchange factor
T	Temperature
u	Velocity in vertical direction of plumes and ceiling jets
v	Velocity in the radial direction of plumes and ceiling jets; velocity perpendicular to the ceiling in the impingement region
Y_i	Mass fraction of species i
y	Vertical distance measured downward from the ceiling surface
z	Axial coordinate of plumes
α	Entrainment coefficient defined in Equation (3.17)
α_c	Entrainment constant defined in Equation (5.13)
α_o	Constant in Equation (3.30)
β	Coefficient of thermal expansion
δ	Jet width at which the fluid velocity equals 1% of the maximum velocity difference across the flow
ε	Dissipation rate of turbulence kinetic energy

1. Introduction

The present investigation is considering the impingement of fires and fire plumes on a horizontal ceiling. The objective of the research is to study radiative and convective heat transfer rates to the ceiling, as well as the structure of the flow. The approach used in the study involves measurements of heat transfer rates and flow structure. In addition, theoretical models of the process are also considered, as a means of correlating and interpreting the measurements. References 1 and 2 are earlier reports of progress for the study.

Three main regions of the flow can be specified when a fire or fire plume impinges on a ceiling, as follows: 1) the plume, prior to impingement, which defines the initial condition of the process; 2) the stagnation point region, where there are significant pressure variations and boundary layer approximations do not apply; and 3) the ceiling-jet region, where the flow spreads radially along the ceiling with a boundary layer structure. In general, the ceiling jet region is observed for $r/H > 0.2$ [1-5].* The present investigation considers processes in all three regions.

Thermal plumes and fire plumes have attracted substantial attention in the past, e.g., Refs. 6-18, to name only a few. In spite of this effort, however, there have been very few studies of the flame structure above natural fires. The recent studies of Cox and Chitty [12] and McCaffrey [13] are a notable exception. These investigators provide measurements of mean temperatures and velocities in flames produced by a gas-fueled burner. The entrainment properties of fires are another important property which has been addressed during recent work by Zukoski, et. al. [14].

There have been numerous attempts to model the properties of natural fires, employing both simplified integral models as well as detailed field models. Recent integral models are typified by the work of Wilcox [15] and Taminini [16]. The current field models are based on higher-order turbulence models (k-ε or k-ε-g) [10,11,17,18]. Such models have been calibrated using measurements in plumes [10,11,18], and evaluated based on radiative properties [17].

Past studies of impingement on ceilings have been primarily concerned with plume impingement on an unconfined ceiling. Alpert [3,4] has developed an integral model describing this flow, and also provides some data on ceiling heat transfer rates and temperature and velocity levels in the ceiling-jet region. Zukoski, et. al., [5] report additional heat transfer rate data for the same flow. Work on fire impingement on ceilings is largely limited to the earlier results of this investigation [1,2,19]. These findings provide empirical correlations of convective heat transfer rates for cases where the flames extend along the ceiling up to half the ceiling height.

---

*Numbers in brackets denote references.

In all previous work involving flame impingement on a ceiling, measurements of the structure of the flow have been very limited. This has been a great impediment to developing a better understanding of the heat transfer properties of the process. Another limitation of present knowledge concerning natural fires is that past theories have been compared to peripheral properties, such as radiant emission or visible flame length [15-17]. Predicting radiation in turbulent combusting flows represents a significant theoretical problem in its own right, even when the flow structure is known; therefore, it is difficult to obtain a convincing evaluation of a model in this manner. The significance of visible flame length with respect to flow properties, which influence heat transfer rates to surfaces such as temperature and velocity, is questionable.

In view of this status, the major objective of the present investigation was to complete detailed measurements of the structure of fires impinging on a horizontal ceiling. This includes profiles of mean velocity, temperature and composition, as well as velocity fluctuations. Heat transfer measurements were also completed, including convective heat transfer rates to the ceiling and radiative heat transfer rates from the fire to both the ceiling and the surroundings.

This information was employed to evaluate models of the plume and the ceiling-jet regions, considering the effect of combustion. Both differential and integral models were examined in the plume region. Since the main emphasis of the investigation was to obtain new experimental information, little effort was devoted to development of the differential model. In this case a k-ε-g model developed and successfully evaluated for flows where buoyancy effects are small [20-23] was simply compared with the new measurements. Greater effort was devoted to developing a unified integral model, applicable to combusting flows in both the plume and ceiling-jet regions.

In the following, the experimental apparatus is described first of all. This is followed by a description of the theoretical models for the plume, and their evaluation using the measurements of both this investigation and earlier work. The report concludes with a description of the ceiling-jet model and its evaluation with measurements.

2. Experimental Methods

2.1 Apparatus

Reference 2 provides an extensive description of the experimental methods used during the study. Therefore, only a brief discussion of the apparatus and instrumentation will be undertaken here.

Figure 1 is a sketch of the apparatus. The fire was fueled by natural gas, flowing from a cylindrical burner tube. The natural gas was largely methane, the exact composition appears in Table 1. The burner tube had an inside diameter of 55 mm and was packed with stainless

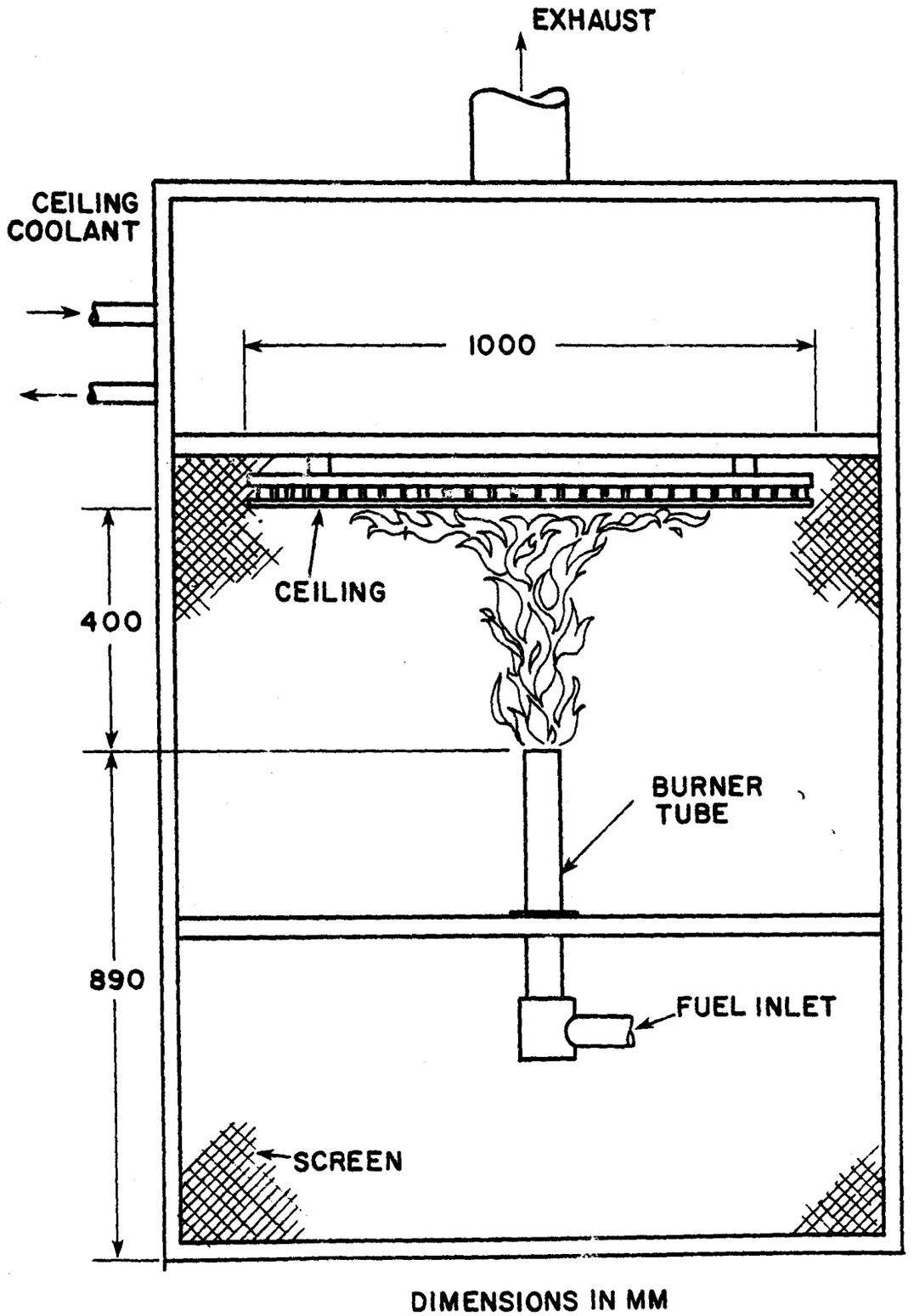

Figure 1. Sketch of the steady-state apparatus for fire impingement on a horizontal ceiling.

Table 1

Composition of Fuel Gas

Species	Percent by Volume
Methane	94.863
Ethane	3.753
Propane	0.266
Iso-Butane	0.039
n-Butane	0.047
Iso-Pentane	0.019
Mono-Sulfur	0.009
Di-Sulfur	0.012
Mercaptans	0.016
n-Pentane	0.016
Hexane	0.084
Nitrogen	0.408
Carbon Dioxide	0.423
Neo-Pentane	0.006
Hydrogen Sulfide	0.019
Hydrogen	0.020

steel wool and screens in order to provide a uniform exit velocity [2]. The test flames attached naturally at the exit of the burner.

A water-cooled ceiling, 1000 mm in diameter, was positioned concentrically with the burner tube, 400 mm above its exit. The water coolant was recirculated from a large drum, maintaining the ceiling within a few degrees of the ambient temperature. The ceiling surface was coated with a high emissivity (0.96) paint. An enclosure above the ceiling collected the flow, which was removed by a natural draft exhaust system.

The apparatus was surrounded by a screened enclosure in order to reduce room disturbances. The enclosure consisted of a single layer of screen (630 wires/m, 0.25 mm wire diameter). No floor was provided at the level of the fire source. Eliminating the floor helped to steady the flame and improved access. The absence of a floor has not been found to influence the structure of natural fires to a great degree [13].

2.2 Instrumentation

Mean velocity, velocity fluctuations and Reynolds stress in the plume region were measured with a dual-beam forward scatter laser-Doppler anemometer (LDA), similar to earlier work on open jets and flames in this laboratory [22,23]. The LDA incorporated a Bragg cell frequency shifter so that flow reversals could be detected near the edge of the flow. Effects of flame luminosity were minimized by employing an optical filter in front of the detector. The optical system was mounted rigidly for these measurements. The LDA measuring volume was positioned in the flame by moving the burner tube (which was mounted on a milling machine vise providing a position accuracy of 1 mm). The optical arrangement yielded an ellipsoidal measuring volume with major and minor diameters of 6.6 and 0.27 mm, respectively. For present test conditions, this results in gradient broadening errors estimated to be less than 10 percent, for both mean and turbulent quantities.

Difficulties were encountered in obtaining adequate seeding levels for the LDA. In the upper portions of the flames sufficient soot was present for seeding and low mixture fractions reduced biasing errors. Near the base and edge of the flames, however, it was necessary to supplement this natural source of particles. Additional particles were provided in high mixture fraction regions using a small acetylene diffusion flame as a particle generator. Near the edge of the flow, an oil particle generator (averaged particle diameter 0.6 μm) was used for this purpose [22].

The LDA system was not satisfactory in the ceiling-jet region. Difficulties were encountered in accurately moving the apparatus, maintaining adequate seeding levels, and avoiding motion of the measuring volume due to density fluctuations and long beam lengths through the flow. Therefore, an impact-static probe was used for the velocity measurements in the ceiling jet. This probe was similar to

the arrangement used by Ahmad and Faeth [24] for wall plumes. The static probe compensates for hydrostatic pressure variations both at the measuring location and in the thermal path of the tubing. The pressure differential was measured with an electronic manometer.

Mean temperatures were measured with 50 μm diameter Pt/Pt-10% Rh thermocouples. The thermocouple junction was formed by butt-welding the wires. The fine wires were mounted to heavier leads spaced 12 mm apart, and aligned normal to the direction of the maximum temperature gradient, in order to reduce conduction errors. The thermocouple probe was moved with a linear positioner, accurate to 1 mm. Even though the thermocouple wires were relatively small, radiation from the flame and to the surroundings was significant, due to the low velocity of the flow. The magnitude of these errors was estimated, and is presented along with the temperature measurements. These estimates are based on a range of thermocouple emissivities, since the thermocouples became tarnished with use. The radiative heat flux measurements were used to estimate flame radiation to the thermocouple near the edge of the flow.

The mean composition of gaseous species (CH_4, H_2, CO_2, CO, H_2O, O_2 and N_2) was measured by isokinetically sampling the flow at the mean gas velocity. The probe was moved with a linear positioner, identical to the temperature probe. The sampling probe has a 2 mm internal bore and was water-cooled. The coolant temperature was maintained at 360 K to avoid condensation of water vapor in the probe. The gas mixtures were analyzed using a gas chromatograph. Calibration experiments were conducted at several positions in the flames in order to determine the effect of gas sampling rates on the measurements. This indicated that sampling velocities within $\pm 50\%$ of the correct mean velocity had little influence on the composition measurements.

Flame shape, defined as the visible luminous edge of the flame, was measured in two ways. In both cases, the flame was observed in a darkened room. The first method involved photographing the flame with a still camera (4 x 5 Graphlex camera employing Polaroid, Type 52 film with a 40 ms exposure time). Ten photographs were obtained for each flame. The photographs were analyzed to yield the mean position of the flame edge and the 95% confidence interval (using Student's t distribution) as a function of height above the burner. The second method involved positioning pointers at the maximum and minimum flame positions, at various distances above the burner, as described in Reference 2. In this case, the flame edge was taken to be the arithmetic average of these two limits.

Heat transfer rates to the ceiling were measured with heat flux gauges. The gauges were mounted flush to the surface, centered under cooling passages. The surface of the gauges were coated with either gold foil, for a convective heat flux measurement, or a black-coated foil, for a total heat flux measurement. Subtracting these measurements yielded the radiative heat flux to the ceiling.

The radiant heat flux from the flame to the surroundings was measured with a gas-purged, water-cooled sensor (Medtherm Radiation Heat Flux Transducer, Type 64F-10-22, 150° viewing angle). In the plume, the sensor was mounted near the edge of the flame and directed toward the axis. Measurements were obtained at various axial stations. In the ceiling-jet region, the sensor was mounted normal to the ceiling at the edge of the flow.

3. Theory--Plume Region

3.1 Differential Model

3.1.1 Description of Model

The model considers a steady, axisymmetric, turbulent flame in an infinite, stagnant media. Analysis of the flow generally follows the procedure developed by Lockwood and coworkers [20,21]. Earlier work in this laboratory [22,23] has demonstrated good results with this approach for forced flows. This includes the study of Shearer, et al., [22] for forced constant and variable density jets in still air. Shearer [22] found good agreement between predicted and measured mean and turbulent quantities, using the model constants recommended by Lockwood and Naguib [20]. Subsequent comparisons for a forced combusting n-propane jet, using the same model constants, were also satisfactory [23]. These results provided a calibration of the model for relatively high Reynolds number flows where buoyancy effects were small. Therefore, the model serves as a useful reference for examining the present flames, where these effects should be more significant.

It is assumed that the boundary layer approximations apply. Flow velocities are low; therefore, viscous dissipation and kinetic energy are ignored in the mean flow equations. Typical of most models of turbulence [20-23], the exchange coefficients of all species and heat are assumed to be the same. Local chemical equilibrium is also assumed at each point in the flow.

In order to reduce the number of empirical parameters to be specified, limiting cases are considered with respect to radiation. The first limit involved ignoring radiant heat losses entirely, similar to Mao, et al., [23]. The second limit is based on the observation of Markstein [25] that the total radiant power of a flame is nearly proportional to its rate of chemical energy release. Therefore, we assume that the flame is optically thin and that a fixed fraction of the chemical energy released by reaction is radiated to the surroundings. This fraction, 20%, was selected to bound the radiant heat losses measured for the present flames.

Under these assumptions, the mixture fraction is a conserved property of flow. For negligible radiation, the instantaneous properties at each point in the flow correspond to the thermodynamic state attained when an amount f of fluid from the burner tube and

(1-f) of ambient fluid, at their initial states, are adiabatically mixed and brought to thermodynamic equilibrium at the ambient pressure of the flow. This general approach is also applied to the second radiation limit, after assuming that the fixed fraction of the chemical energy released during equilibration is lost.

3.1.2 Equation of State

With the above assumptions, an equation of state can be constructed once and for all, for each radiation limit. The equation of state provides instantaneous flow properties, e.g., temperature, composition and density, as a function of mixture fraction. Construction of the equation of state involves completing conventional flame equilibrium calculations for various mixture fractions. In the present case, ideal gases are assumed, allowing for variable specific heats and dissociation. The calculations are completed using the package computer program CEC-72 [26]. This program incorporates JANNAF thermochemical properties for the combustion gases. The fuel used in the test flames is predominantly methane, c.f. Table 1, and is approximated as pure methane. The ambient composition is approximated as dry air. Both reactants are assumed to have an initial temperature of 300 K, with equilibration occurring at atmospheric pressure.

Construction of the equation of state requires some rather arbitrary decisions concerning the extent of equilibration. Low and high mixture fractions are outside normal flammability limits. Furthermore, unreasonable quantities of soot are predicted for mixture fractions near unity. Similar to earlier work [23], complete equilibrium is assumed for mixture fractions less than 0.08. For higher mixture fractions, the formation of soot and the equilibration of the water-gas reaction is inhibited. Recent measurements by Mitchell, et al., [27] suggest that the water-gas reaction is not equilibrated for equivalence ratios greater than two in typical methane diffusion flames, tending to support this approach. In addition, it is not possible to reconcile the mean temperature and mixture fraction measurements at high mixture fractions for the present flames without inhibiting the water-gas reaction.

Figure 2 is an illustration of the equation of state for the present test flames, at the limit of no radiant heat loss. Temperature, density, and the mass fractions of methane, nitrogen, oxygen and the major product species are plotted as a function of mixture fraction. The equation of state for 20% radiative heat loss is qualitatively similar. The major change involves a reduction of mixture temperature (a maximum of 290 K at the stoichiometric mixture ratio) and a slight increase in density, at each mixture fraction.

3.1.3 Governing Equations

Similar to past studies [20-23], the turbulent flow model involved the solution of Reynolds-averaged conservation equations. Mean quantities are obtained by solving conservation equations for mass,

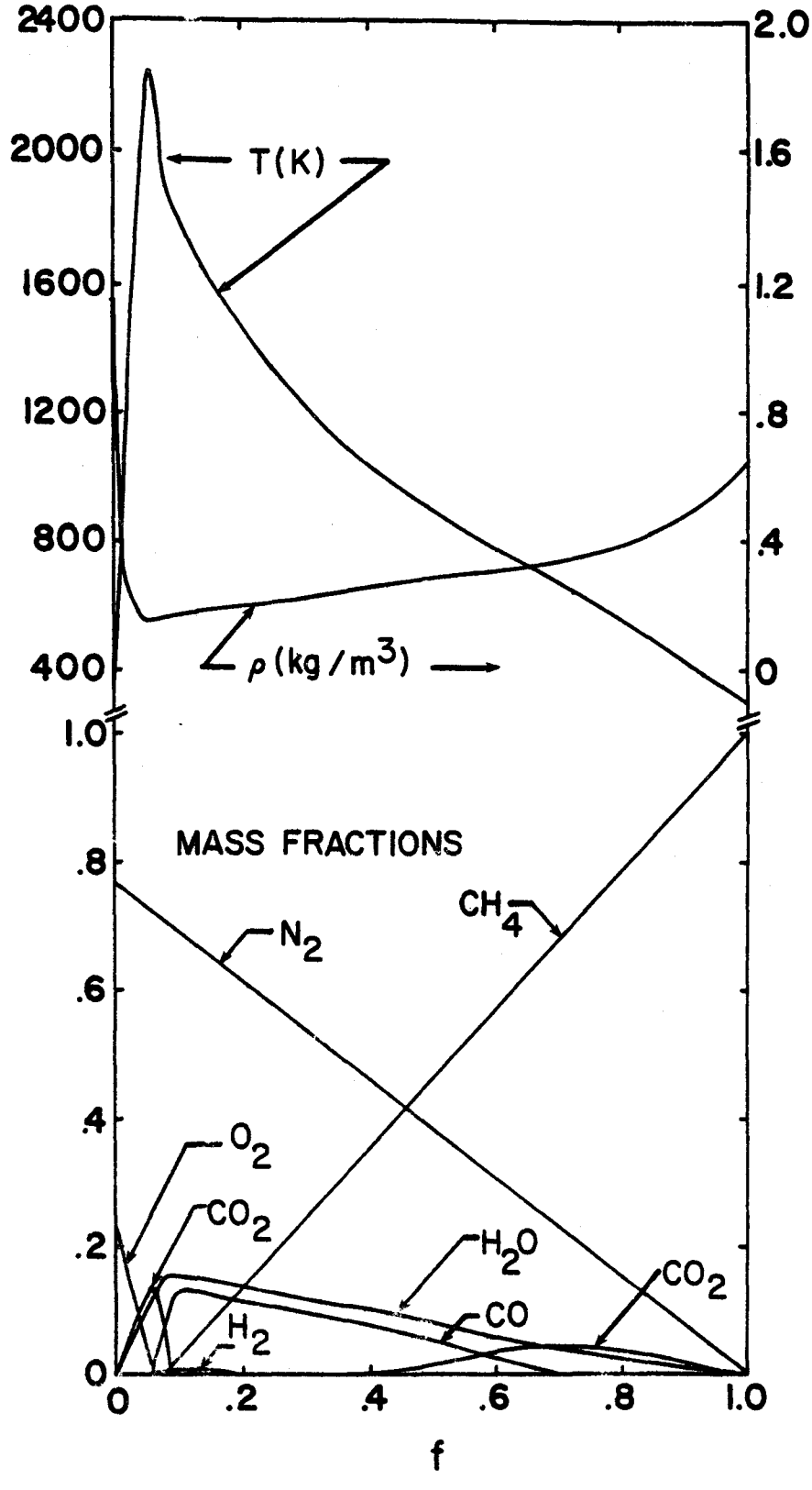

Figure 2. Equation of state for methane combustion in air at atmospheric pressure (reactants initially at 300 K and no radiant heat loss).

momentum and mixture fraction. Turbulence characteristics are found by solving model transport equations for turbulence kinetic energy, dissipation, and concentration fluctuations. With this approach, several terms involving density fluctuations are ignored, for lack of better information. The justification for this approach rests on the success of the method for a number of variable density flows [20-23]. While buoyancy is considered in the mean equations, its effect on turbulence quantities is ignored. The details of the development of the governing equations follows the approach outlined by Gosman, et al., [21].

With these assumptions, the governing equations are as follows:

$$\frac{\partial \bar{\rho}\bar{u}}{\partial z} + \frac{1}{r}\frac{\partial}{\partial r}(r\bar{\rho}\bar{v}^{o}) = D(\bar{u}) - a(\bar{\rho}_{\infty} - \bar{\rho}) = D(\bar{f}) = 0 \tag{3.1}$$

$$D(k) = \mu_t \left(\frac{\partial \bar{u}}{\partial r}\right)^2 - \bar{\rho}\varepsilon \tag{3.2}$$

$$D(\varepsilon) = C_{\varepsilon 1}\mu_t \frac{\varepsilon}{k}\left(\frac{\partial \bar{u}}{\partial r}\right)^2 - C_{\varepsilon 2}\bar{\rho}\frac{\varepsilon^2}{k} \tag{3.3}$$

$$D(g) = C_{g1}\mu_t \left(\frac{\partial \bar{f}}{\partial r}\right)^2 - C_{g2}\bar{\rho}\frac{\varepsilon g}{k} \tag{3.4}$$

where

$$\bar{\rho}\bar{v}^{o} = \bar{\rho}\bar{v} + \overline{\rho' v'} \tag{3.5}$$

$$\mu_t = C_{\mu}\bar{\rho}k^2/\varepsilon \tag{3.6}$$

and

$$D(\phi) = \bar{\rho}\bar{u}\frac{\partial \phi}{\partial z} + \bar{\rho}\bar{v}^{o}\frac{\partial \phi}{\partial r} - \frac{1}{r}\frac{\partial}{\partial r}\left(r\frac{\mu_t}{\sigma_{\phi}}\frac{\partial \phi}{\partial r}\right) \tag{3.7}$$

for $\phi = \bar{u}, \bar{f}, k, \varepsilon$, or g.

The parameters C_i and σ_i appearing in Equations (3.1)-(3.7) are constants. Two sets of constants are examined during the present calculations. Their values are summarized in Table 2. Set i corresponds to the values which were employed during calibration of this model [20-23], where best results were obtained using the original recommendations of Lockwood and Naguib [20]. Set ii corresponds to values used in recent work by Lockwood and coworkers [22]. The individual values of the two sets of constants are not very different, with $C_{\varepsilon 2}$ and C_{g2} and $\sigma_f = \sigma_g$ in both cases.

3.1.4 Computations

The mean value of any scalar quantity (other than $\bar{f}$, k, ε, g and μ_t) is computed as a weighted average, as follows:

$$\phi = \int_0^1 \phi(f) \; P(f) \; df \tag{3.8}$$

The equation of state, e.g., Figure 2, provides $\phi(f)$. P(f) is the probability density function for f, which is chosen to be a clipped Gaussian function and defined by the following equations:

$$P(f) = \frac{1}{\sigma(2\pi)^{1/2}} \exp[-1/2(\frac{f-\mu}{\sigma})^2] \quad , \quad 0 < f < 1 \tag{3.9}$$

$$P(0) = \int_{-\infty}^{0} \frac{1}{\sigma(2\pi)^{1/2}} \exp[-1/2(\frac{f-\mu}{\sigma})^2] \; df \tag{3.10}$$

$$P(1) = \int_{1}^{\infty} \frac{1}{\sigma(2\pi)^{1/2}} \exp[-1/2(\frac{f-\mu}{\sigma})^2] \; df \tag{3.11}$$

where μ is the most probable value and σ is the variance of the distribution [20-23]. These parameters can be found from $\bar{f}$ and g, which are known as a result of integrating Equations (3.1) and (3.4). Lockwood and Naguib [20] described the entire procedure in some detail.

The calculations are begun at a position 100 mm above the exit of the burner, using measured properties at this station for initial conditions. This approach is chosen since the region near the burner

Table 2

Constants in the Turbulence Model

Set[a]	C_μ	$C_{\varepsilon 1}$	C_{g1}	$C_{\varepsilon 2} = C_{g2}$	$\sigma_f = \sigma_g$	σ_k	σ_ε
i.[b]	0.09	1.44	2.8	1.84	0.7	1.0	1.3
ii.[c]	0.09	1.57	2.8	1.92	0.9	1.0	1.3

[a] $\sigma_u = 1$, by definition.

[b] Employed in References [20, 22, 23] for variable density flows.

[c] Employed in Reference [21] (except for $C_{\varepsilon 2} = C_{g2} = 1.82$ and 1.90).

exit, where the flame contracts as the flow accelerates, is not a boundary layer flow. Effects of laminar flow and transition, which have not been incorporated into the model, were also observed near the exit of the burner.

This choice of the initial condition eliminates the need for consider the development of a shear layer at the edge of the flow, near the exit of the burner. Throughout the region that is considered, appropriate boundary conditions for Equations (3.1)-(3.7) are as follows:

$$r = 0 \ , \ \frac{\partial \phi}{\partial r} = 0 \quad ; \quad r \to \infty \ , \quad \phi = 0 \tag{3.12}$$

At the initial condition, the measurements give complete profiles of $\bar{u}$, $\bar{f}$, $\overline{u'^2}$, $\bar{T}$ and the $\bar{Y}_i$. This provides the initial values of $\bar{u}$, and $\bar{f}$ immediately; however, initial values of k, ε and g must be estimated.

The initial values of k were estimated from the velocity fluctuation measurements. For isotropic turbulence $k = \overline{3'^2}/2$, while computations for noncombusting plumes suggest that $k = \overline{u'^2}$ [18]. The latter value is used in the calculations due to the general similarity of buoyant plumes and natural fires.

The initial value of ε is obtained by estimating the value of the turbulent viscosity, and employing this estimate, along with k, to compute ε from Equation (3.6). Seeding difficulties limit the reliability and availability of Reynolds stress measurements at the initial condition; therefore, the turbulent viscosity is estimated using Prandtl's mixing length theory. That is

$$\mu_t = \bar{\rho} \ \ell_m^2 \ \left|\frac{\partial \bar{u}}{\partial r}\right| \tag{3.13}$$

For a round jet [28], the mixing length is

$$\ell_m = K\delta \tag{3.14}$$

Where K = 0.075 and δ is the width at which the fluid velocity equals 1% of the maximum velocity difference across the flow. Combining Equations (3.13) and (3.14) with Equation (3.6) yields the following initial estimate for ε

$$\varepsilon = 16k^2/(\delta^2 \left|\frac{\partial \bar{u}}{\partial r}\right|) \tag{3.15}$$

Since ε is expected to be finite near the plume center, the ε at this position is limited by [28]

$$\varepsilon = k^{3/2}/\ell_m \tag{3.16}$$

The initial value of g is estimated using the measurements of $\bar{f}$, and $\bar{T}$. Given $\bar{f}$ at a location, and the equation of state, $\bar{T}$ can be computed as a function of g using Equation (3.8). The values of g which match predicted and measured values of $\bar{T}$ are employed for the initial condition.

The method of solution is similar to earlier work [22,23], utilizing a modified version of GENMIX. The computations employed thirty-three cross-stream grid nodes, with a maximum axial step size corresponding to the minimum of either 2% of the current radius of the flow, or the position where the entrained flow is 10% of the current flow. Reduction of these parameters had no significant effect on the results.

3.2 Integral Model

3.2.1 Description of Model

The objective of the integral model was to provide a simplified approach for analyzing plume properties, which could be extended to treat the properties of the ceiling jet. The general approach is similar to other integral models already proposed for this problem [15,16]. The major differences involve the assumption of "top hat" profiles, and the manner of treating entrainment, reaction and radiation. These changes were made to simplify the computations as much as possible while still maintaining the essential elements of the flow process. Some compromises were also dictated by the need to ultimately extend the approach to the ceiling-jet region.

The major assumptions of the model are:

1. The fire plume is steady and axisymmetric with zero mean swirl.
2. The fire plume is a boundary-layer-type flow.
3. Pressure is constant at each cross-section of the fire plume.
4. The ideal gas law is valid.
5. The surroundings are homogeneous and stagnant.
6. Kinetic and potential energies are negligible
7. Properties are uniform across the width of the flow ("top hat" profiles).

3.2.2 Governing Equations

With these assumptions, the governing equations have the following form:

$$\frac{d}{dz}(\sigma^2\bar{\rho}\bar{u}) = 2\alpha\sigma\rho_\infty\bar{u} \tag{3.17}$$

$$\frac{d}{dz}(\sigma^2\bar{\rho}\bar{u}^2) = \alpha(\rho_\infty - \bar{\rho})\ \sigma^2 \tag{3.18}$$

$$\frac{d}{dz}(\sigma^2\bar{\rho}\bar{u}\bar{Y}_i) = \bar{P}_i\ \sigma^2 + 2\alpha\sigma Y_{i\infty}\ \bar{u}\ \rho_\infty \tag{3.19}$$

$$\frac{d}{dz}\ [\sigma^2\bar{\rho}\bar{u}\bar{C}_p\ (\bar{T} - T_r)]$$

$$= 2\alpha\sigma\rho_\infty C_{p\infty}\ \bar{u}\ (T_\infty - T_r) + 2\int_0^\sigma Q_R r dr - 2\ \sum_i \bar{P}_i h_i^{(o)} \tag{3.20}$$

where the entrainment constant α is defined as [29]

$$\alpha = (\bar{v}_e)_{r=\sigma}/\bar{u} \tag{3.21}$$

and $(v_e)_{r=\sigma}$ is the radial entrainment velocity at the plume edge.

The quantities σ, $\bar{u}$, $\bar{Y}_i$, and $\bar{T}$ are defined by neglecting the axial transport by turbulence. The quantities on the left-hand side of Equations (3.17)-(3.21) represent the following integrals:

$$A_1 = \sigma^2\bar{\rho}\bar{u} = 2\int_0^\infty \rho u r dr \tag{3.22}$$

$$A_2 = \sigma^2\bar{\rho}\bar{u}^2 = 2\int_0^\infty \rho u^2 r dr \tag{3.23}$$

$$A_3 = \sigma^2\bar{\rho}\bar{u}\bar{Y}_i = 2\int_0^\infty \rho u Y_i r dr \tag{3.24}$$

$$A_4 = \sigma^2\bar{\rho}\bar{u}\bar{C}_p\ (\bar{T} - T_r) = 2\int_0^\infty \rho u C_p\ (\bar{T} - T_r)\ r dr \tag{3.25}$$

where $C_p = \Sigma_i Y_i C_{p_i}$.

Then $\bar{u}$, $\bar{Y}_i$, $\bar{T}$ and σ can be calculated from the following relationships:

$$\bar{u} = A_2/A_1 \tag{3.26}$$

$$\bar{Y}_i = A_3/A_1 \tag{3.27}$$

$$\bar{T} = A_4/\bar{C}_p A_1 + T_r \tag{3.28}$$

$$\sigma = (A_1 / \pi\bar{\rho}\bar{u})^{1/2} \tag{3.29}$$

where $\bar{\rho}$ can be calculated by knowing the concentration, $\bar{Y}_i$, and the temperature, $\bar{T}$.

3.2.3 Computations

In order to solve Equations (3.17)-(3.20), the functions α, $\bar{P}_i$ and Q_R have to be specified.

For strongly buoyant plumes Morton [29] suggested that the entrainment coefficient is

$$\alpha = \alpha_o(\bar{\rho}/\rho_\infty)^{1/2} \tag{3.30}$$

where α_o is an empirical constant.

Equation (3.30) predicts little entrainment near the source, where velocities are low. For combusting fires, however, experience indicates that entrainment near the source is vigorous due to the rapid variation of velocity in this region. In order to account for the acceleration near the source, Wilcox [15] proposed

$$\alpha = \alpha_o(\bar{\rho}/\rho_\infty)^{1/2}[1+(K/\alpha_o)\sigma d\ln \bar{u}/dz] \tag{3.31}$$

where both K and α_o are empirical constants. Equation (3.31) will be used in the present model.

The basic hypothesis used to specify the rate of reaction follows the turbulent reaction model developed by Magnussen and Hjertager [30]. This assumes that chemical reaction rates are fast in comparison to the rate of mixing between fuel-rich and oxygen-rich eddies and that turbulent mixing is controlled by the rate of dissipation of eddies. Fuel and oxidizer are also assumed to react in stoichiometric proportions. For the present case, where methane is burned in stagnant air, we have the following stoichiometry

$$CH_4 + 2(O_2 + 3.76\ N_2) \rightarrow CO_2 + 2H_2O + 7.52\ N_2 \tag{3.32}$$

The rate of combustion is then expressed as [30],

$$\bar{P}_{CH_4} = -\ C_R\ \bar{\rho}\ \{\bar{Y}_{CH_4}\ ,\ \bar{Y}_{O_2}/r_f\}\ \varepsilon/k \tag{3.33}$$

where { } stands for the minimum of the two quantities in brackets, and r_f is the stoichiometric mass ratio of oxygen to methane. This form is posed since the rate of reaction should be controlled by the species which is present in the smallest amount [30].

Invoking the mixing length hypothesis and assuming that the turbulence is fully developed, the dissipation, ε and k, can be approximated as follows:

$$\varepsilon \sim u'^3/\ell_m \quad ; \quad k \sim u'^2 \tag{3.34}$$

Then

$$\varepsilon/k \sim u'/\ell_m \tag{3.35}$$

Since the flow is fully developed, the width σ is proportional to the distance ℓ_m. Then we get the following expression for the consumption rate of methane

$$\bar{P}_{CH_4} = -\ C_R\ \bar{\rho}\ \{\bar{Y}_{CH_4}\ ,\ \bar{Y}_{O_2}/r_f\}\ \bar{u}/\sigma \tag{3.36}$$

where C_R is an empirical constant which must be evaluated experimentally.

The consumption rate of oxygen and production rates of water vapor and carbon-dioxide are related by the following stoichiometric relationships

$$-\frac{\bar{P}_{CH_4}}{Mv_{CH_4}} = -\frac{\bar{P}_{O_2}}{2Mv_{O_2}} = \frac{\bar{P}_{CO_2}}{Mv_{CO_2}} = \frac{\bar{P}_{H_2O}}{2Mv_{H_2O}} \tag{3.37}$$

Radiation was treated using two methods. First of all, parallel to the turbulence model, it was assumed that some fixed percentage of the reaction energy is lost by radiation. In this case, the radiation loss is simply

$$2\int_0^{\sigma} Q_R \, rdr = \sigma^2 \eta_r \sum_i \bar{P}_i \, h_i^{(o)} \tag{3.38}$$

where η_r represents the fractional loss of energy of reaction due to radiation.

The other method employs the exponential-wide-band model of Edwards, et al. [31] to calculate the radiation loss. Assuming that the flame is optically thick in the axial direction, we have the following results from Siegel and Howell [32]:

$$2\int_0^{\sigma} Q_R \, rdr = -2\sigma \sum_{k=1}^{K} \pi D_k S g_k [I_{b,k}(\bar{T}) - I_{b,k}(\bar{T}_e)] \tag{3.39}$$

where $I_{b,k}$ is the black-body spectral intensity which is calculated from the following expression

$$I_{b,k}(\bar{T}) = 2C_1 \nu_k^3 / [\exp(C_2 \nu_k / \bar{T}) - 1] \tag{3.40}$$

where

$$C_1 = 0.59544 \times 10^{-12} \text{ W - cm}^2$$

$$C_2 = 1.4388 \text{ cm - K}$$

and ν_k is the spectral wave number.

The initial conditions required to integrate Equations (3.17)-(3.20) are provided by the flow at source exit. A rational extrapolation procedure is used to integrate the equations [33]. The constants K and α_o in the entrainment function were obtained by matching predictions with available data on weakly buoyant plumes and fire plumes. The parameter C_R is the function for reaction rate was determined by matching predictions with the present measurements.

4. Results and Discussion--Plume Region

4.1 Test Conditions

Two test conditions were employed for the measurements of flame structure. The operating conditions for these flames are summarized in Table 3. Radial profile measurements were completed at distances of 100, 215 and 300 mm above the exit of the burner. Axial profile measurements spanned the range from 100 to 350 mm. The maximum temperature along the axis was at 120 mm for Flame I; therefore, these results emphasized the upper portions of a natural fire. The maximum temperature along the axis was at 270 mm for Flame II; therefore, in this case the test range covered the lower portions of the flame. The data: flame shape, mean temperature, radiant heat flux, mean velocity, fluctuating velocity, Reynolds stress, and species concentration, are tabulated elsewhere [34].

Flame boundaries measured by visual observation are a subjective matter. Variations result from the sensitivity of the experimenter's eyes, the degree of luminosity of the flame, the brightness of the background, and the geometry of the flame. The present results were measured in a darkened room (by H-Z. Y.). Repeatability of maximum and minimum flame locations was within 5%.

Errors in the LDA measurements are due to the following broadening effects: finite transit time of the particles, velcoity gradients, velocity fluctuations, and fluctuations in the position of the measuring volume due to density fluctuations. The total error from these broadening effects was estimated to be less than 15% [34].

Due to the radiation, the temperature in the center of the flame was underestimated; however, the temperature was overestimated near the edge. Analysis indicated that errors in temperature measurements could reach 200 K in the center region, while the error was 1-5 K at the edge.

Several independent measurements were made of each quantity to test repeatability of the measurements. Repeatability was within the following limits: mean velocity, 5%; mean temperature, 6%; mean concentration, 15%; velocity fluctuations, 11%; Reynolds stress, 20%; flame radiation flux, 7%; and mean flame position, 5%. Rechecking measurements over a period of months also yielded results within these limits.

Table 3

Summary of the Natural Gas Diffusion Flames[a]

Flame	I	II
Fuel flow rate (mg/s)	34.1	174.0
Heat release rate (kW)	1.67	8.51
Burner exit velocity (m/s)	0.0210	0.1073
Burner exit Reynolds Number[b]	70	356
Burner exit Richardson Number[c]	1222	46.8
Free flame height (mm)	350	710
Height of maximum temperature along axis (mm)	120	270
Flame tip Rayleigh Number[d]	1.64×10^{12}	3.35×10^{13}

[a]Vertical burner with 55 mm ID, containing an array of stainless steel screens (45 mm apart, 3940 wires/m, square pattern, 0.10 mm wire diameter) with a similar screen spot-welded across the burner exit. Ambient condition was still air at 294-300 K, 97-99 kPa. Fuel was natural gas at 294-300 K.

[b]$= u_o D/\nu_o$

[c]$= aD/u_o^2$

[d]$= a\beta_\infty \dot{Q} L^2/\rho_\infty C_{p\infty} \nu_\infty^3$

Conservation of mass was also examined in order to check the measurements. This involved integrating the measurements across the flow to yield the mass flow rate of material originating from the burner, as well as the mass flow rates of elemental carbon, hydrogen, oxygen and nitrogen. The integrations employed measurements of mean velocity, temperature and composition. The results are summarized in Table 4, where the burner flow rate, the ratio of the mass flow rates of elemental carbon and hydrogen, and the ratio of the elemental flow rates of oxygen and nitrogen are provided for each test location. The last quantity can be compared to the composition of air (neglecting the relatively small oxygen and nitrogen concentrations of the fuel, and the small amounts of water vapor and carbon dioxide in air). The maximum discrepancy between the expected and measured value of a quantity is 42%, for the measured fuel flow rate of Flame I at x = 300 mm. The error is largest here, since the composition of fuel and combustion products is lowest at this condition, which maximizes composition errors. Checks of the remaining parameters agree with expectations within 20-30%. Repeated measurements and checking test procedures were unable to improve these results. The main reason for the discrepancies is felt to be errors near the edge of the flow, where concentrations of fuel and combustion products are low leading to reduced accuracy for the composition measurements. Errors near the edge of the flow are magnified in a conservation of mass check, since even low concentrations can yield significant flow rates of material, due to the relatively large flow area of this region. Effects of axial turbulent transport [9], time averages as opposed to Favre averages, seeding difficulties, and varying humidity of the ambient air are also factors contributing to the error.

4.2 Comparison of Differential Model Predictions and Measurements

Flame boundaries for the two test flames are illustrated in Figures 3 and 4. Results for both the visual and the photographic methods are shown as bounds, due to the fluctuating nature of the flow. The photographs were obtained using a Graphlex 4 x 5 still camera (Polaroid Type 52 film, f = 4.7 with an exposure time of 40 ms). Any other setting would result in a shift of the photographic flame boundaries. This exposure time was chosen to roughly correspond to the time constant of the human eye. For these conditions, the flame shape found from the photographs was generally narrower than the shape obtained from direct visual observation.

Gas velocities leaving the burner are relatively low, in order to simulate a natural fire. Therefore, the flame radius contracts near the burner exit, as the flow accelerates due to buoyancy forces. A minimum flame radius is reached about one burner radius above the burner exit. Above this region, the flame radius grows again, in response to the radial growth of the flow as a result of entrainment. The maximum flame radius in the plume portion, occasionally reaches r/z = 0.4, for both flames.

Table 4

Mass Conservation Balances of Flame I and Flame II

x(mm)	$\dot{m}_F$ (mg/s)[a]	$\dot{m}_C/\dot{m}_H$[b]	$\dot{m}_{O_2}/\dot{m}_{N_2}$[c]
Flame I:			
0[d]	34.1	3.07	0.304
100	27.7	2.10	0.346
215	24.8	3.41	0.319
300	19.9	3.33	0.316
Flame II:			
0[d]	174.0	3.07	0.304
100	120.0	3.19	0.307
215	148.0	3.93	0.288
300	176.0	3.39	0.306

[a]Total mass flow rate of material originating from burner fuel flow.

[b]Ratio of mass flow rates of element carbon to element hydrogen.

[c]Ratio of mass flow rate of element oxygen to element nitrogen.

[d]Burner flow condition, except that of $\dot{m}_{O_2}/\dot{m}_{N_2}$ which is the ratio for dry air.

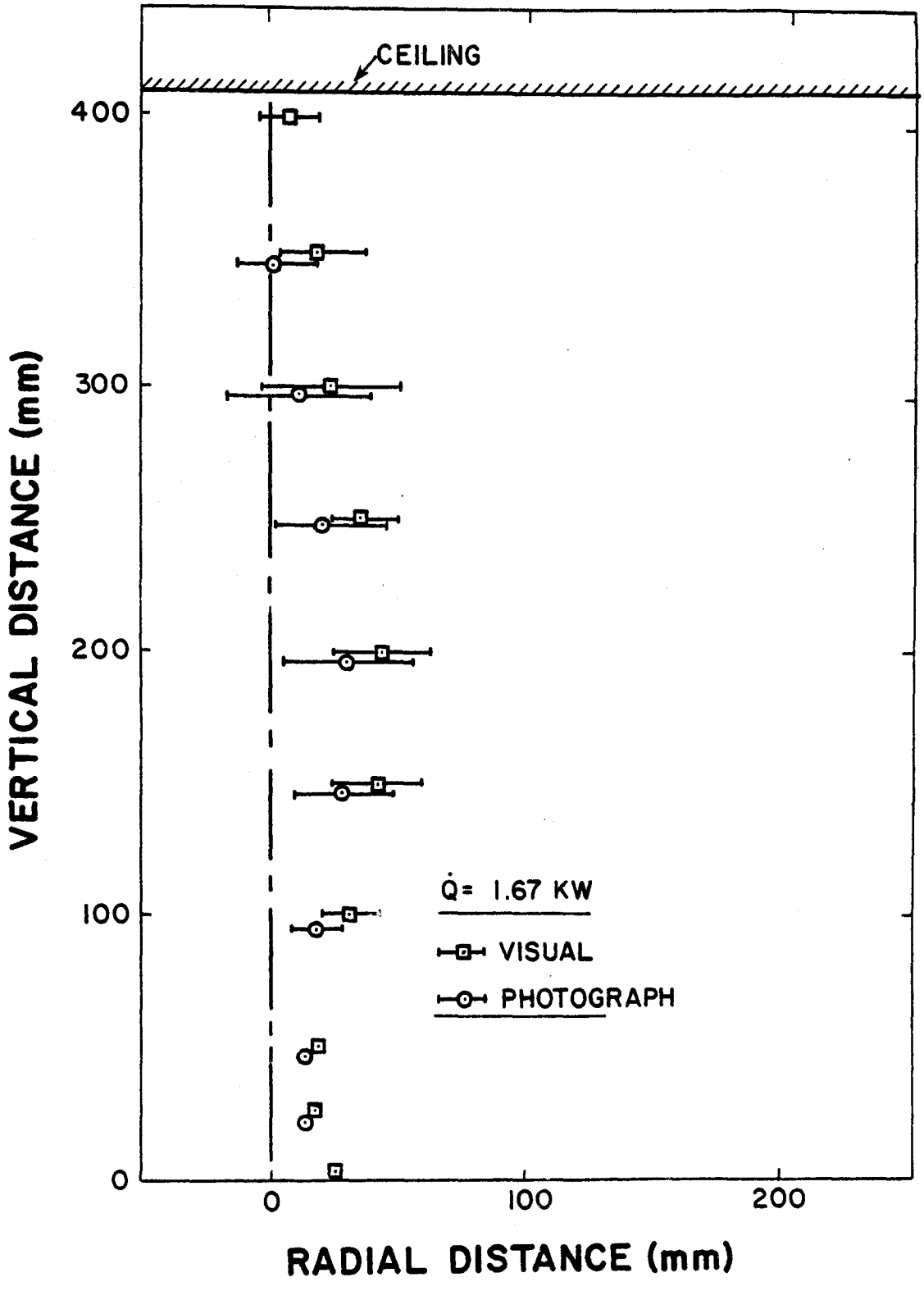

Figure 3. Flame shape, flame I.

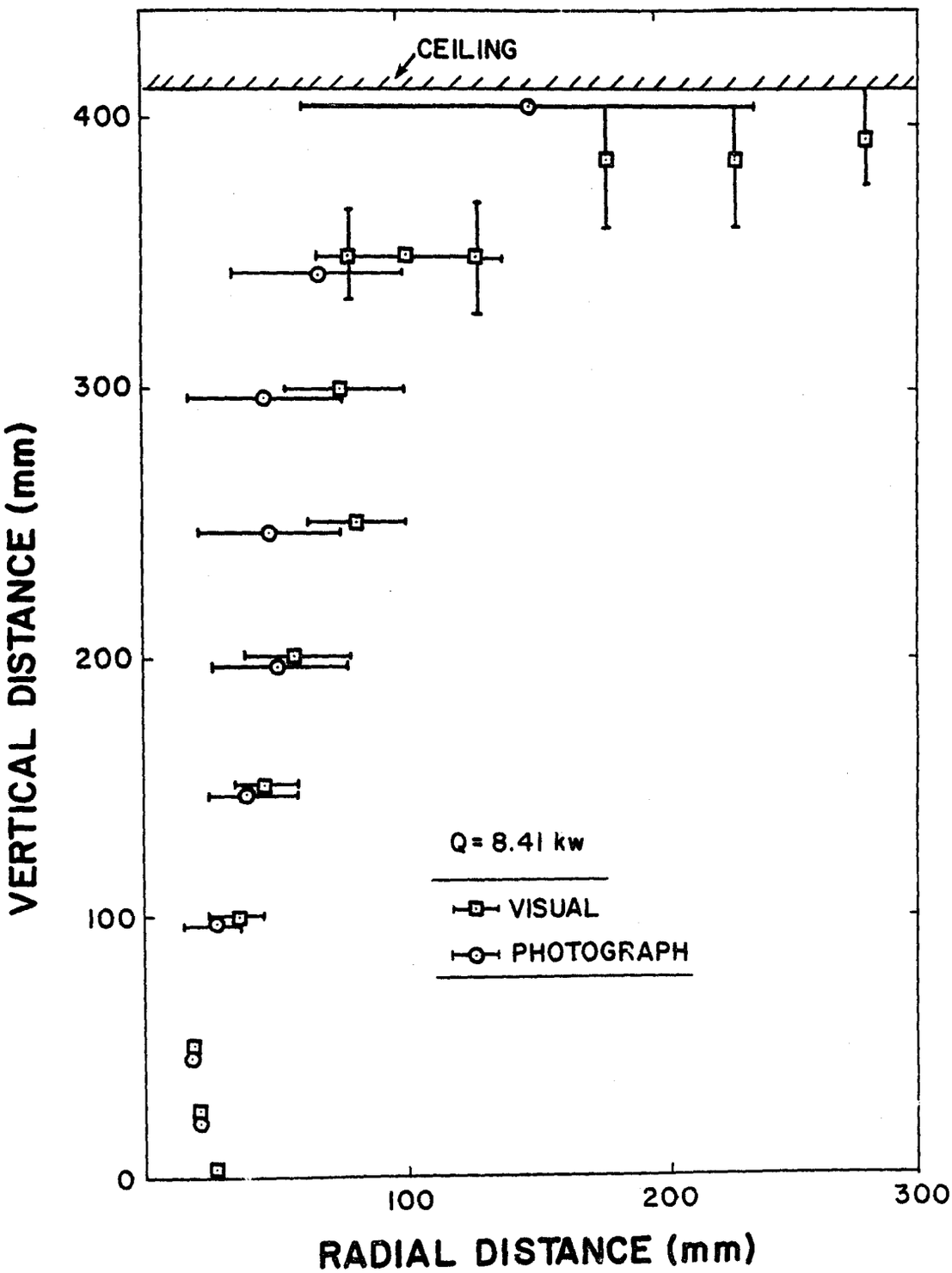

Figure 4. Flame shape, flame II.

The remaining data for the test flames are illustrated in Figures 5-12. Also shown on these figures are the predictions using the two radiation approximations. In order to orient the data with the appearance of the flame, the luminous edge of the flame is indicated on each figure. The axial variation of flame width is illustrated in Figures 6 and 10. In this case, the mean flame position is indicated by the symbol, while the range of the flame position is indicated by bars. For the photographic method, the bars indicated the 95% confidence interval of the measurements. For the visual method the bars indicated the observed maximum and minimum flame positions. In general, the visual technique yields wider flame boundaries. On the remaining figures, the extremities of both methods, combined, are indicated. It can be seen that the outer extremity of the flame generally extends to the edge of the flow as indicated by other measured quantities. The visible portion of the flame also extends well beyond the maximum temperature positions in both the axial and radial directions.

The measured temperatures shown on each figure are not corrected for radiation effects; however, anticipated errors due to radiation are indicated by error bars at a number of positions. Error bars are shown, due to the uncertainty in the emissivity of the thermocouple after a period of exposure to the flame. The error limit farthest from the measurements corresponds to a thermocouple emissivity of unity. In high temperature regions, the thermocouple indication is below the temperature of the flow, with maximum errors of 180 K near maximum temperature locations. Near the edge of the flow, the thermocouple indication is higher than the flow temperature since the sensor intercepts flame radiation. This effect is smaller, yielding errors on the order of 5 K.

The axial variation of radiant heat flux from each flame is illustrated in Figures 6 and 10. The position of maximum radiant heat flux generally coincides with the maximum temperature location along the flame axis. An estimate of a radiant heat loss of 15%, from Flame I, was made by integrating the measured radiant heat flux along the axis. A similar computation could not be made for Flame II, however, since the measurements only covered the lower portion of this flame.

The predictions illustrated in Figures 5-12 employ the model constants of set i summarized in Table 2. Results for both equations of state are shown, with the exception of species concentrations. In the case of species concentrations only results for the equation of state allowing for radiation losses are illustrated, in order to avoid overcrowding the figures. In other instances, where only a single solid line is shown, results for both models overlap. Effects of model constants and the influence of radiant heat losses on species concentration predictions are not large, and will be discussed later.

As noted earlier, k was set equal to $\bar{u}'^2$ at the initial conditions (Figures 5 and 9). For the remaining figures, these two quantities have been plotted together so that they can be compared. Finally, the predicted values of g are also illustrated on the plots. It should be

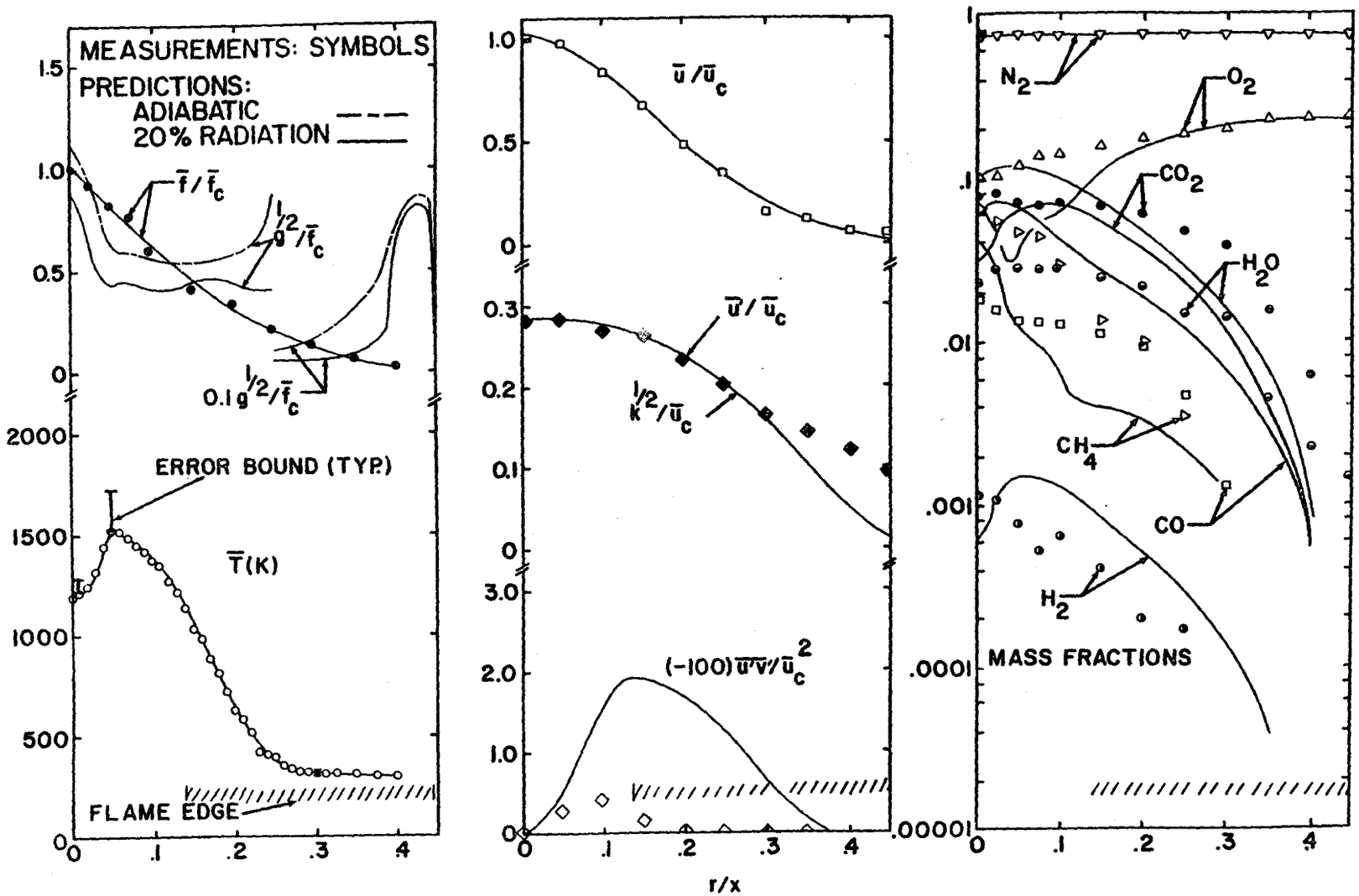

Figure 5. The initial condition for flame I--radial profiles of mean and turbulent quantities at z = 100 mm.

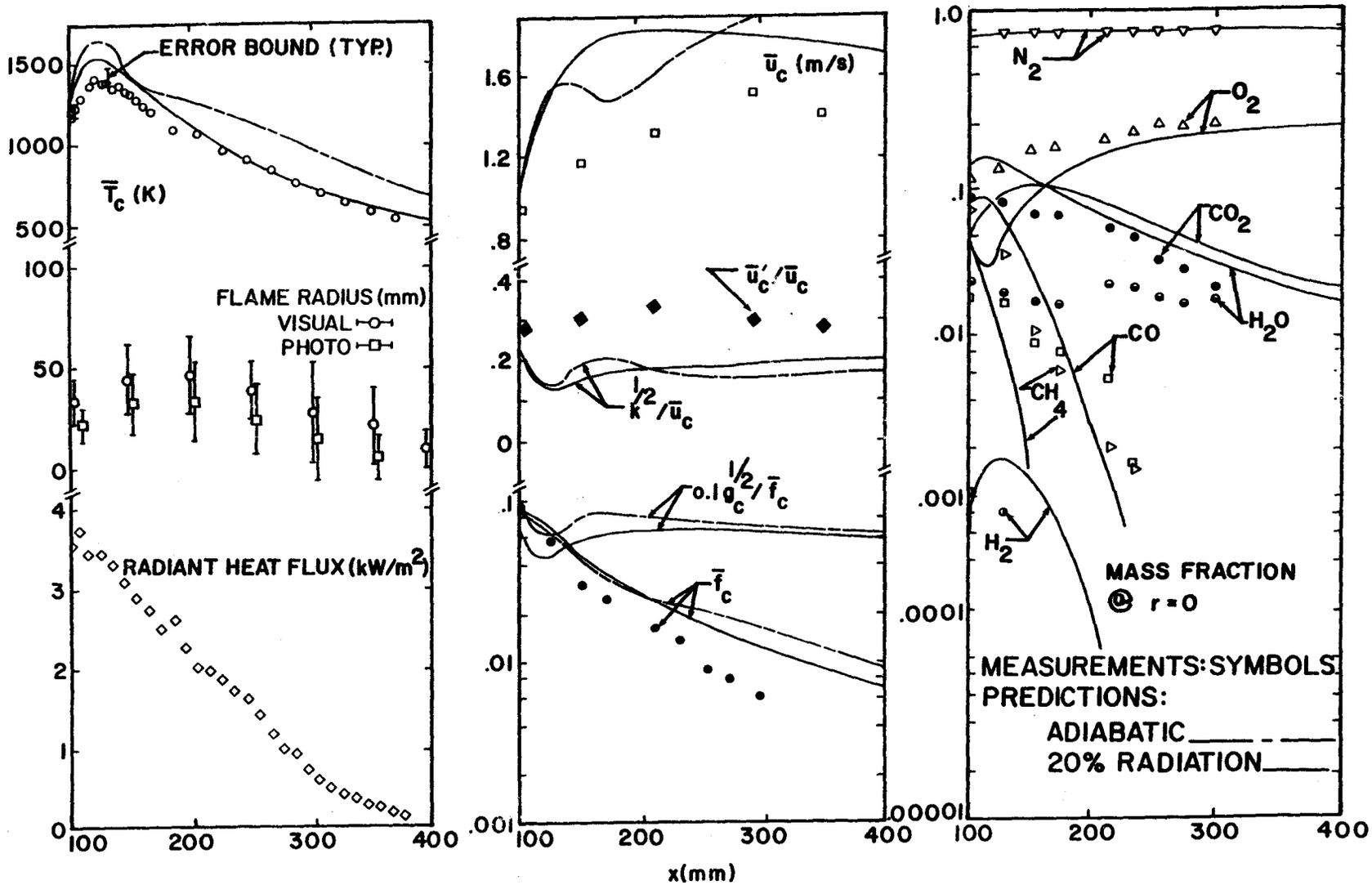

Figure 6. Axial variation of mean and turbulent quantities for flame I.

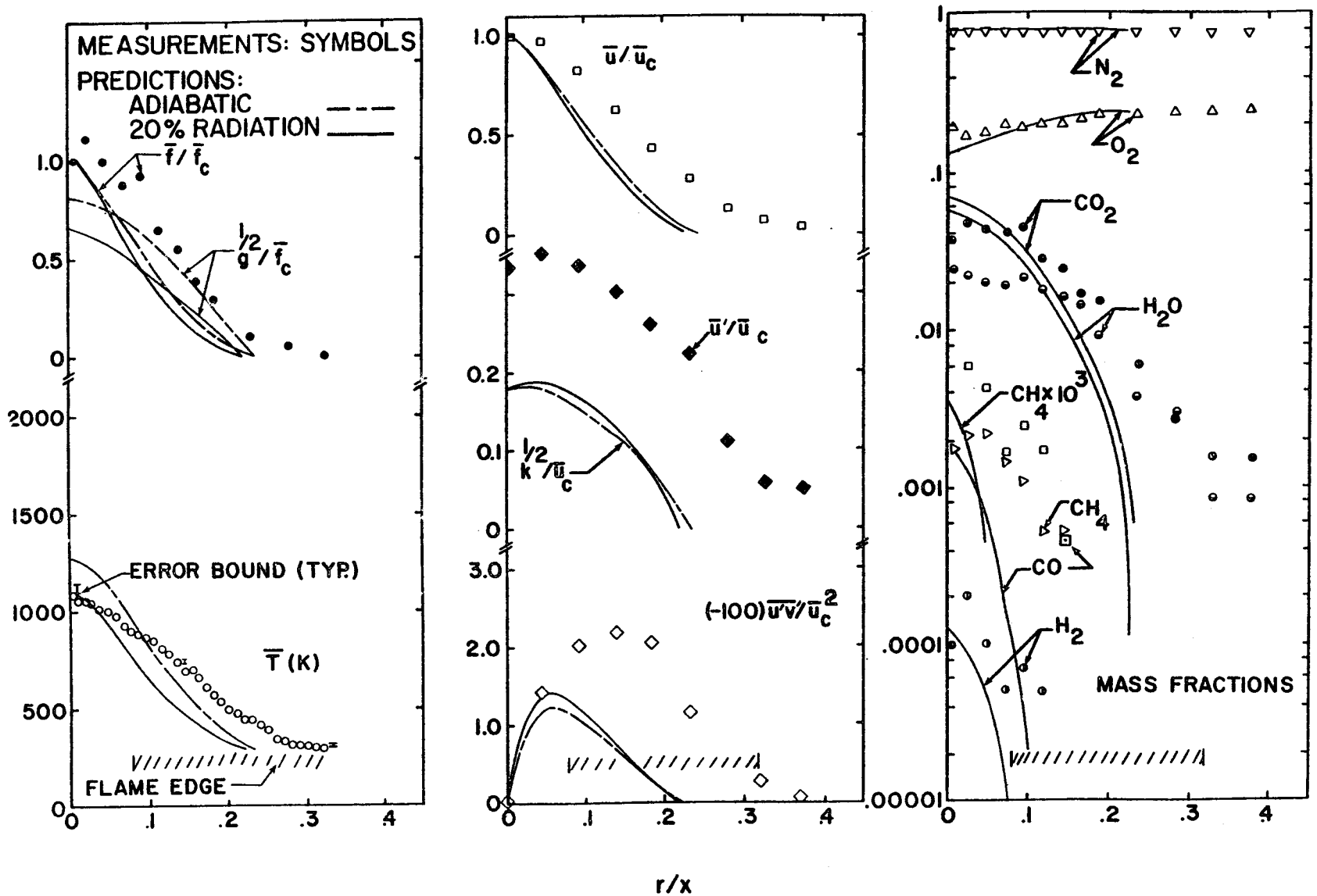

Figure 7. Radial profiles of mean and turbulent quantities for flame I at z = 215 mm.

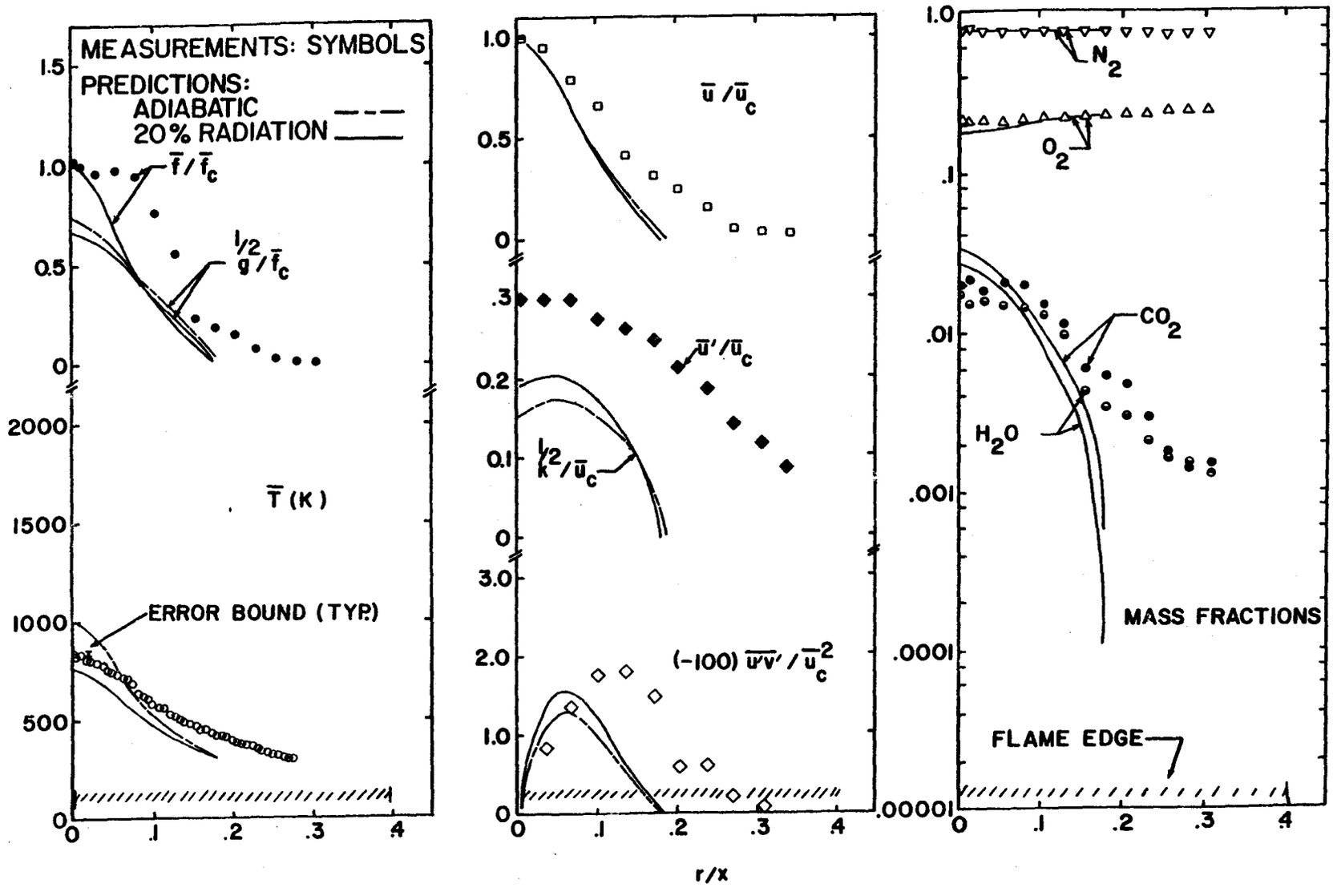

Figure 8. Radial profiles of mean and turbulent quantities for flame I at z = 300 mm.

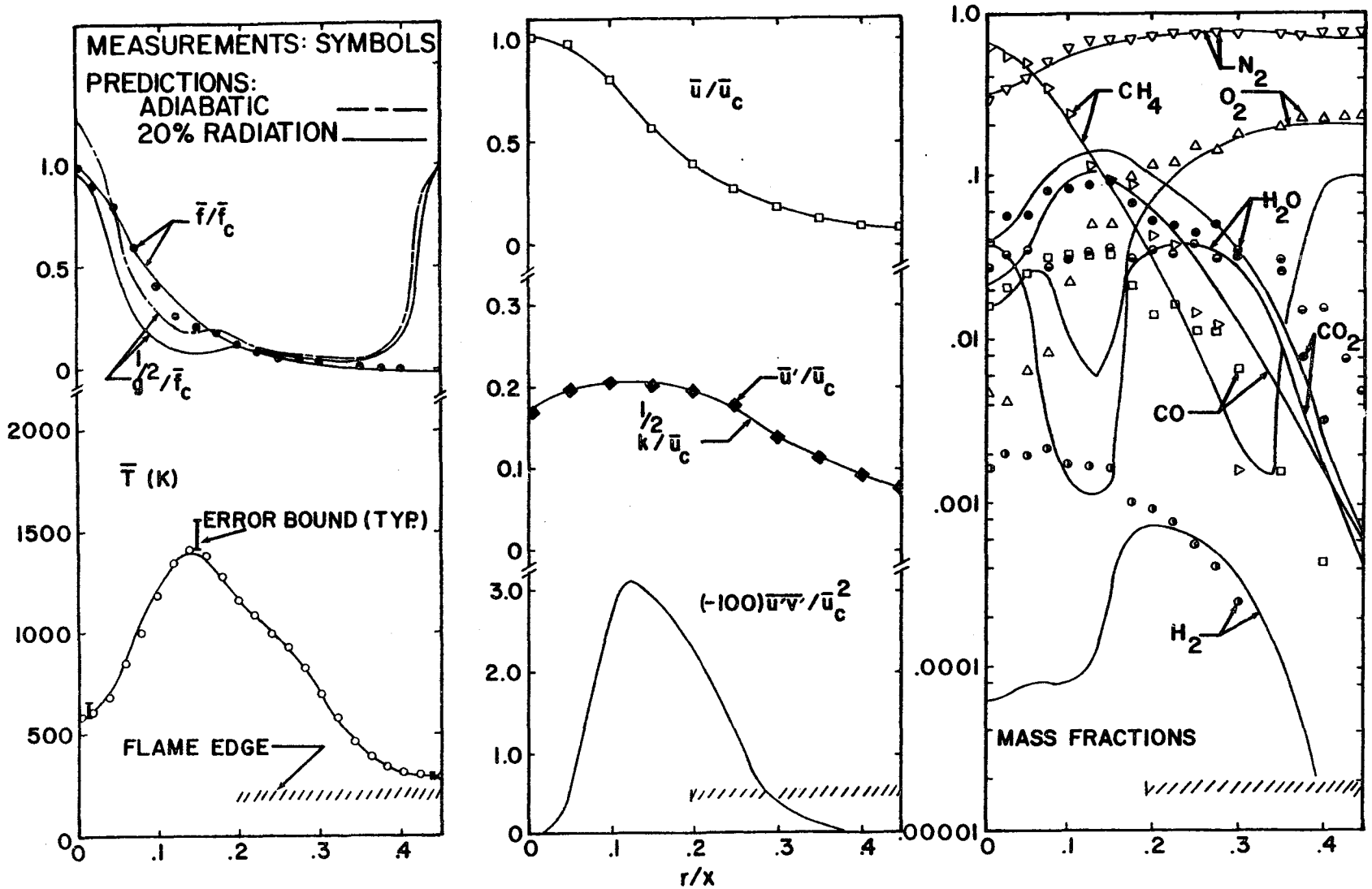

Figure 9. The initial condition for flame II--radial profiles of mean and turbulent quantities at z = 100 mm.

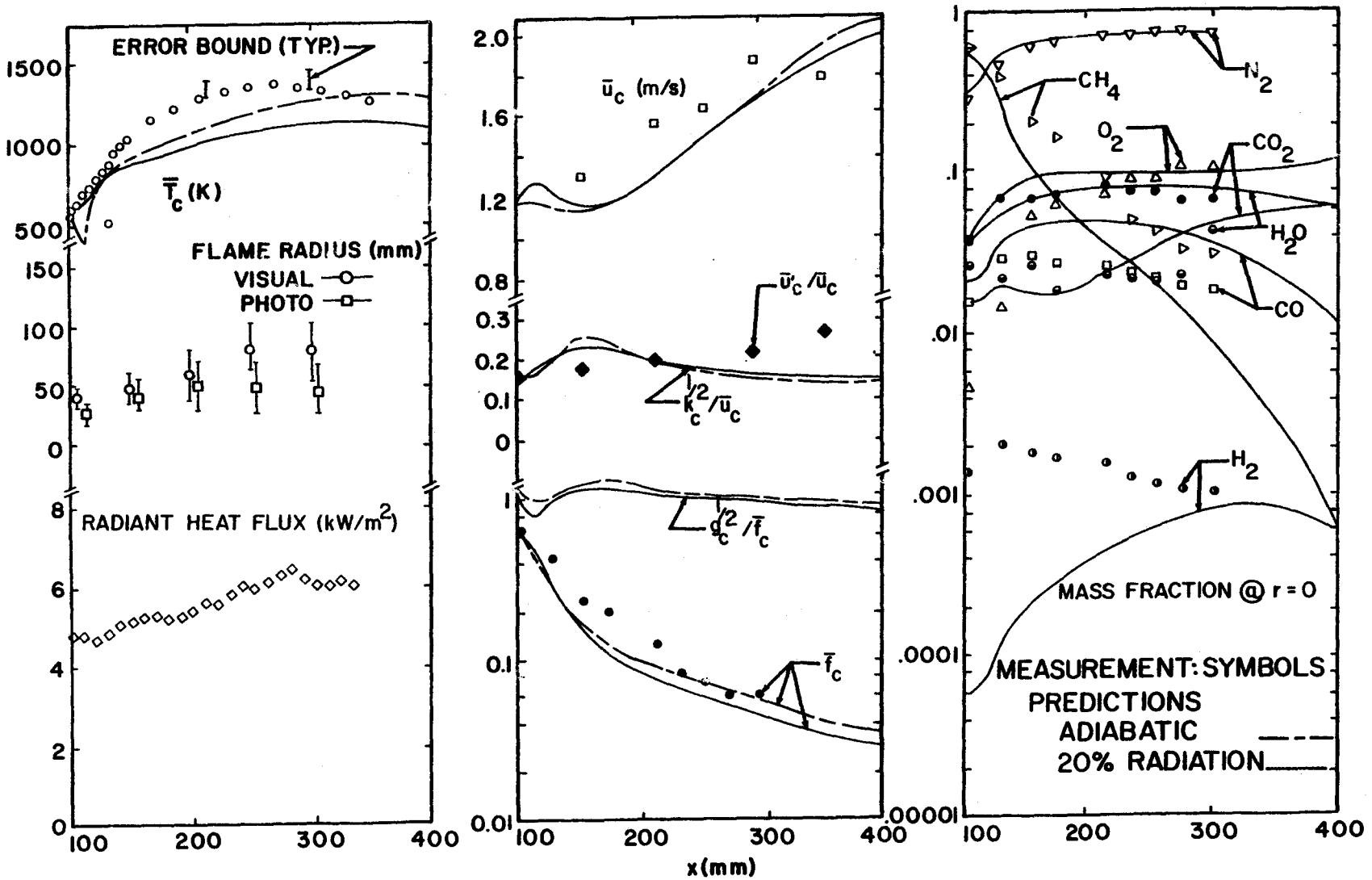

Figure 10. Axial variation of mean and turbulent quantities for flame II.

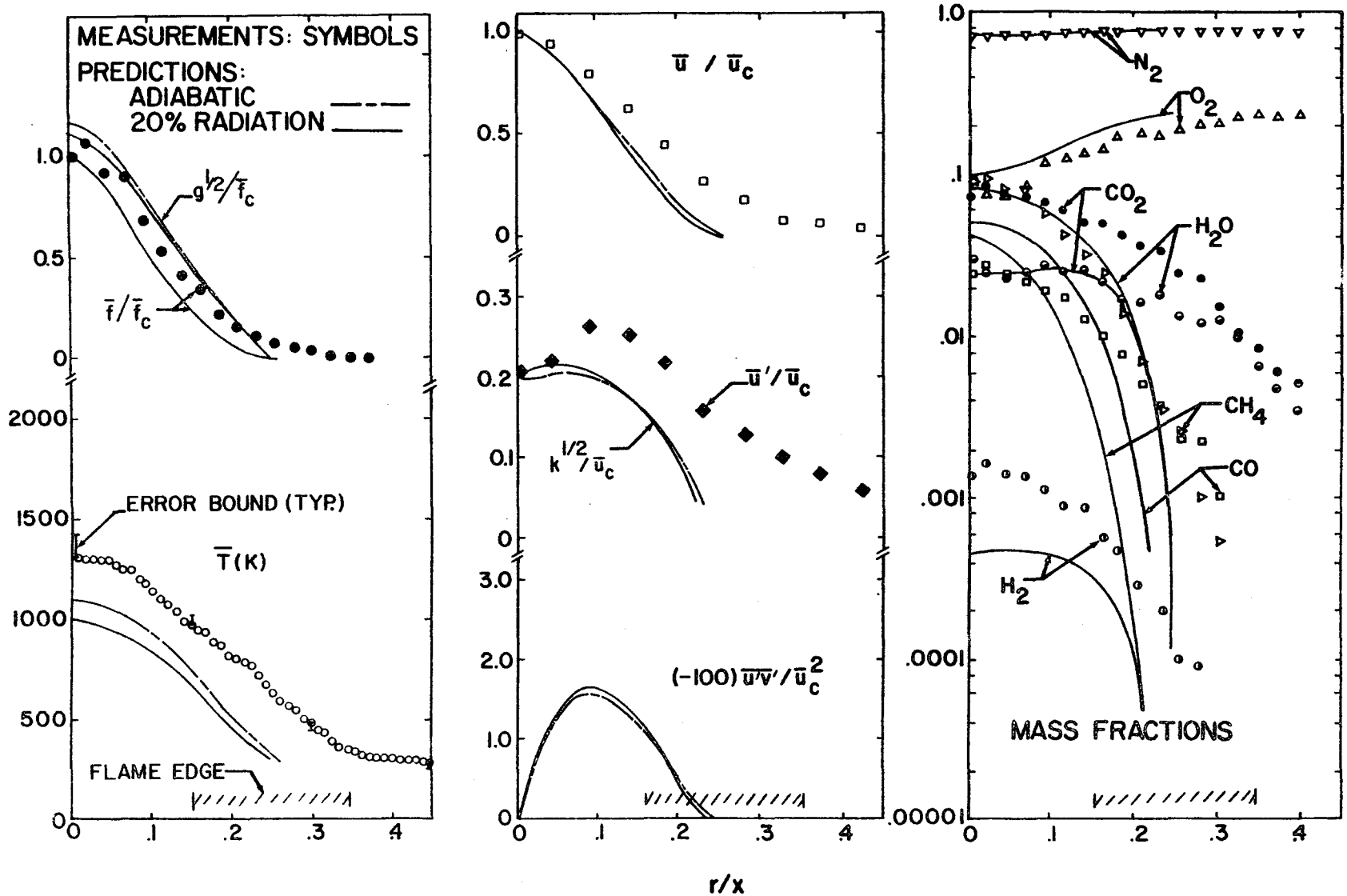

Figure 11. Radial profiles of mean and turbulent quantities for flame II at z = 215 mm.

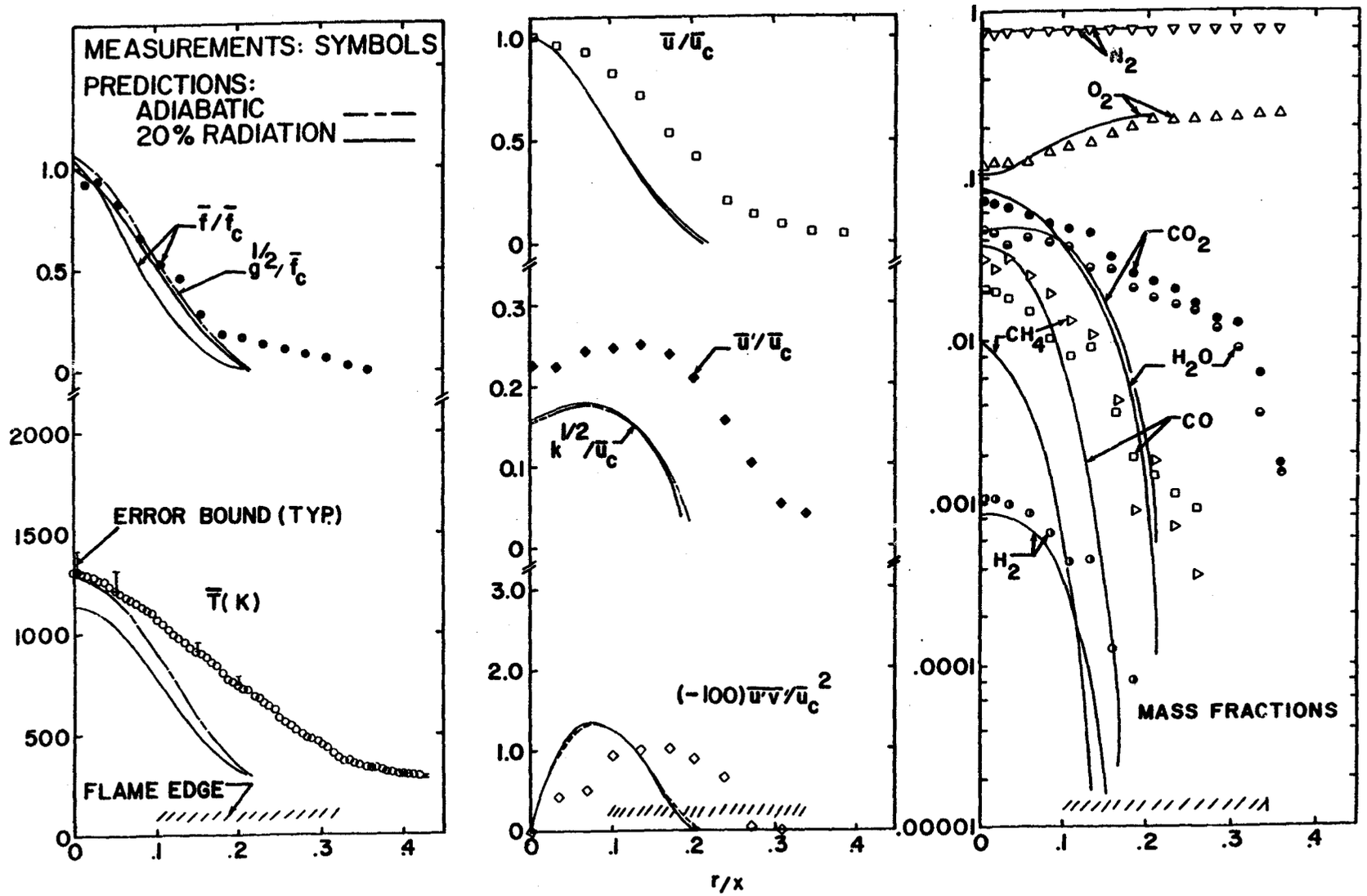

Figure 12. Radial profiles of mean and turbulent quantities of flame II at z = 300 mm.

recalled that g was selected to match the mean mixture fraction and temperature profiles at the initial condition, Figures 7 and 11. For the remaining figures, g was computed by the model.

The values of g required to match initial conditions are too high near the edge and center of the flow, when compared to the usual behavior of concentration fluctuations [18,20]. This effect is probably due to the fact that the uncorrected temperature measurements were matched in the center region of the flow, and mixture fraction f is high near the edge. Near the center of the flow, the actual gas temperature is higher than indicated and an excessively large value of g is needed to lower the predicted temperature.

This effect influences the prediction of mean species concentrations, which were not matched, at the initial condition positions illustrated in Figures 6 and 10. In regions where g values are not normal, largely at the centerline and the edge of the flows, species concentrations exhibit erroneous trends. This initial condition difficulty, however, decays away rapidly, and concentration profiles, as well as g itself, have a more rational behavior at higher locations in the flame. The extent of the predicted flow field influenced by the initial condition for g is seen in the axial profiles illustrated in Figures 6 and 10. The effect is indicated by a jump or oscillation in the predictions which extends to 120-150 mm above the exit of the burner.

Another aspect of estimating parameters at the initial condition involves the Reynolds stress. In the case where Reynolds stress could be measured at the initial condition, Flame I illustrated in Figure 5, the estimated value is substantially greater than the measurements. However, this measurement is felt to be of limited reliability, due to seeding difficulties; therefore, the estimation procedure for the computations was not changed. Nevertheless, the comparison does suggest that development of turbulence characteristics is not complete at the initial condition location for the present flames. Similar to g, Reynolds stress values appear to be more normal at higher positions in the flames.

There is only fiar agreement between predicted and measured quantities along the axis of the flames, Figures 6 and 10, particularly in view of the much better agreement exhibited by this model for forced flows [22,23]. There is little to choose between predictions for the two equations of state, although the model allowing for radiant heat loss does provide a better estimate of mean temperatures in the region beyond the maximum temperature position.

The major discrepancy between predictions and measurements involves the width of the flow. This is particularly evident at the highest position, Figures 8 and 12, where the predicted width is as much as 50% smaller than the measurements. In contrast, this model yielded excellent predictions of flow widths for forced flows [22,23]. Tamanini [17], also encountered similar problems with his predictions of buoyant flames, employing the data of Reference 25, even though he allowed for effects of buoyancy on turbulence properties.

The measurements were also compared with calculations employing set ii of the model constants. These results generally fall in the range of the predictions shown in Figures 5-12. Several different approaches were used to estimate initial conditions, assuming initial profiles of g based on results for plumes [18], etc. Again, these calculations gave results similar to those pictured in Figures 5-12.

Taken as a whole, the agreement between predictions and measurements may be good enough for many purposes, however, there is clearly room for improvement. Models treating the effect of buoyancy on the production and transport of turbulence quantities can possibly provide better predictions. However, such improvements will require the systematic determination of a number of new empirical parameters. Work along these lines, thus far, has not achieved significantly better results than those illustrated here [17]. Comparing the present limiting calculations, including and neglecting radiant heat losses, indicates that flame radiation has a significant influence on flame structure for present test conditions. This suggests that adopting recent methods for treating radiation in flames [21] might improve predictions. Certainly, the values of the model constants could be optimized to improve the agreement between predictions and measurements, at least for present test conditions. The generality of such an approach, however, would be questionable.

Experimental difficulties and the test conditions themselves are also factors in the discrepancies between predictions and measurements. It is very difficult to completely eliminate room disturbances which deflect the flow in a nonturbulent way. The low momentum of these flows and the absence of a surface to help stabilize large scale disturbances magnify the problem. Such disturbances provide an obvious mechanism for unusually wide profiles of flow quantities.

The local Reynolds numbers in the present test flames are also relatively low. In particular, observation suggests that the lower portions of Flame II exhibited patches of laminar flow. In contrast, the turbulence model was developed, and largely calibrated, for high Reynolds number flows. Therefore, some of the discrepancy may be due to transition effects and poorly developed turbulence.

Our inability to completely measure all properties required to specify the initial condition for the computations also leaves uncertainties in the comparison of predictions and measurements. It appears that these effects are limited to the lower portions of the flow, however, the present results do not provide a thorough indication of the extent to which errors in initial conditions influence the computations.

Finally, the measuring techniques introduce uncertainties which are difficult to evaluate quantitatively. Thermocouple errors and seeding difficulties have already been discussed. In addition, the interpretation of average values obtained from the measurements also has an effect. The velocity and temperature measurements approach a

time average using present techniques; however, isokinetic sampling tends to yield a Favre average for compositions [35]. This distinction did not have a large influence on earlier results for forced flows, where initial conditions could be specified at the burner tube exit [22,23]; however, in the present case measured mean temperatures, velocities and compositions (mixture fraction) were employed to fix initial conditions for the computations and the effect should be larger.

In view of these potential error sources and the limitations of the present model, the comparison between predictions and measurements is encouraging.

4.3 Comparison of Integral Model Predictions and Measurements

From experimental results for jets and plumes, obtained far from the source, it is known that the entrainment rate is closely related to the momentum and buoyancy of the jets and plumes. In other words α is a function of the Froude number [36]. Ricou and Spalding [37] found $\alpha = 0.08$ for jets; Rouse, et al., [6] found $\alpha = 0.12$ for a plume generated from a relatively small fire source; Yokoi [8] and George, et al., [9] obtained $\alpha = 0.14$ and 0.153 for plumes generated by fire or heated air from large sources, respectively.

In the combusting region, the entrainment of air is enhanced by the mixing of large eddies and air diffusing to the combustion zone to sustain reaction. Therefore, α is expected to be larger in a combusting flow. The entrainment of air is also very sensitive to ambient disturbances for buoyant plumes. Small environmental disturbances can cause the fire plume to flap which increases the entrainment rate [14]. Finally, the entrainment is influenced by fire strength and source size [14].

Obviously the simple form of Equation (3.30) cannot account for all these effects. In fact, the values of K and α_o tend to vary from case to case. These parameters are chosen in the following to optimize entrainment predictions for fire plumes.

The present integral model was first compared with plume properties in the weakly buoyant plume region. Correlations obtained by Rouse, et al., [6] and Yokoi [8], and the data provided by George, et al., [9] and the present study were used in the comparison. Equations (3.22)-(3.25) were used to determine the "top hat" properties of the various plume measurements.

In order to compare the predictions with the measurements provided by different investigators, the scaling quantities z_r, $\bar{\rho}_r$ and μ_r, developed by Chen and Rodi [10] were used. These scaling parameters are defined as follows:

$$z_r = (D_o^4 Fr^2 \bar{\rho}_o/\rho_\infty)^{1/4}/2 \tag{4.1}$$

$$u_r = (\bar{u}_o^4 Fr^{-2} \bar{\rho}_o/\rho_\infty)^{1/4} \tag{4.2}$$

$$\rho_\infty - \bar{\rho}_r = (\rho_\infty - \bar{\rho}_o) Fr^{-1/2} (\bar{\rho}_o/\rho_\infty)^{-3/4} \tag{4.3}$$

where

$$Fr = \bar{\rho}_o \bar{u}_o^2 / a D_o (\rho_\infty - \bar{\rho}_o) \tag{4.4}$$

Theoretically, the properties of buoyant plumes, when scaled with the parameters defined in Equations (4.1)-(4.4), should be independent of source properties at large distances from the source. In order to check this, two source conditions were employed in the computations: (1) that of George, et al., [9], and (2) that of the helium plume tests conducted during the initial phase of this investigation [2]. In each case properties were assumed to be uniform over the flow cross-section, and the source and flow radii were taken to be the same, at the source.

Figure 13 is an illustration of predictions and measurements treated in this manner. Two sets of entrainment constants, α_o, are illustrated for the predictions, with K = 0.1 in each case. As anticipated, the predicted results are independent of source properties in the region far from the source. Results for $\alpha_o = 0.14$ provide the best agreement between predictions and measurements, although the scatter of the data is appreciable. Use of $\alpha_o = 0.182$ results in a consistent overestimation of plume width and underestimation of velocity and density defect, due to overestimation of the entrainment rate. However, we shall see that the higher value of α_o yields better results for entrainment in the combustion region.

Zukoski, et al., [14] provided the most extensive results for the entrainment of buoyant fires. In this study, entrainment was measured directly by capturing the entire flow in the plume at various heights above the source. This data is recent and is believed to be the most reliable results available: therefore, the values of α_o and K for flames were selected to match these measurements.

The comparison of the predictions with the entrainment data of Reference 14 is illustrated in Figure 14. The measurements are plotted as the mass flow rate of the fire plumes versus the distance from the fire source, normalized by the flame height. The mass flow rate of the

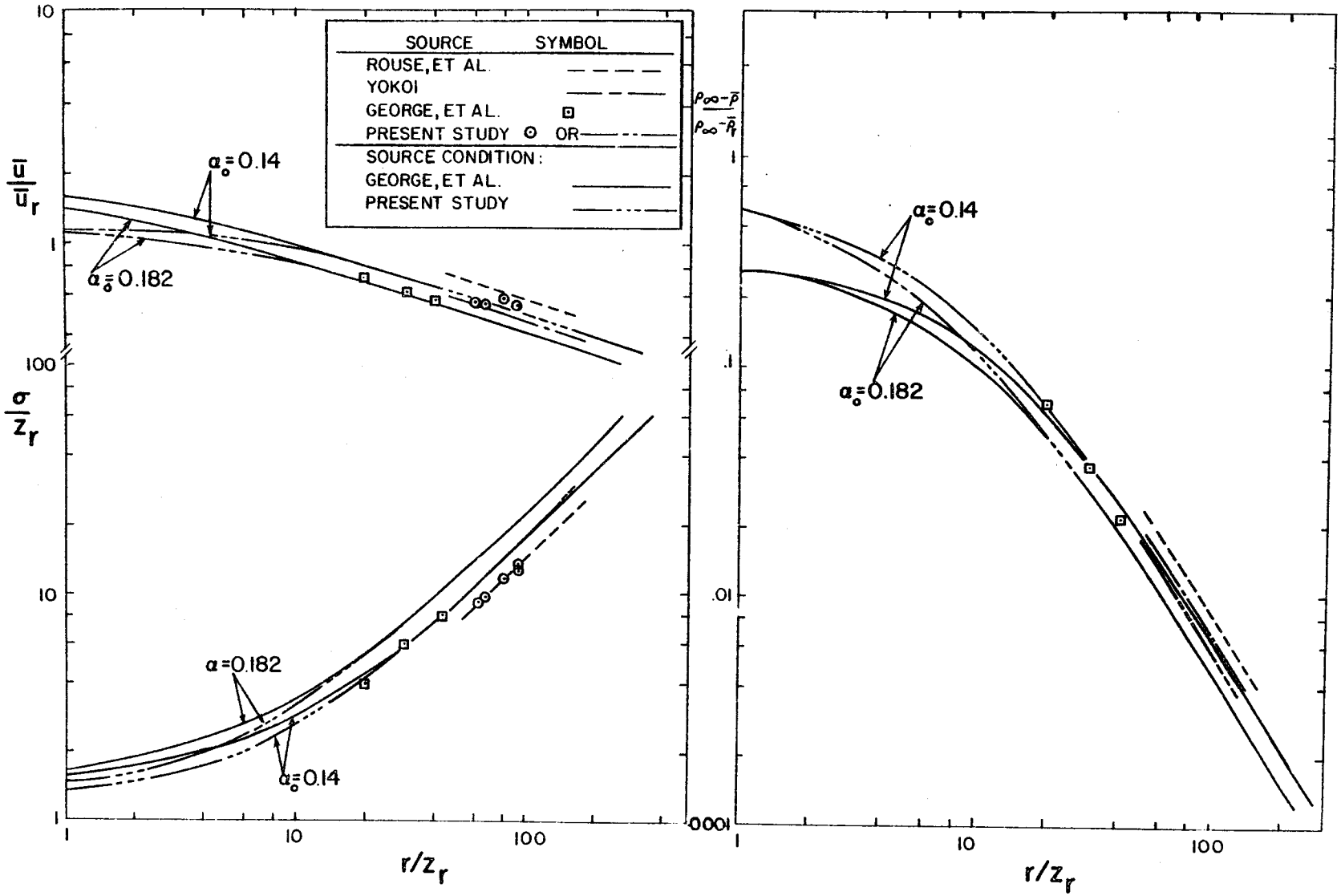

Figure 13. Calibration of the integral model with the data of weakly buoyant plumes.

plume is normalized by the theoretical mass flow rate, which is defined as follows [14]:

$$\dot{m}_{pt} = 0.210\rho_{\infty}(az^5)^{1/2}[\dot{Q}/\rho_{\infty}C_pT_{\infty}(az^5)^{1/2}]^{1/3} \qquad (4.5)$$

$\dot{m}_{pt}$ represents the mass flow rate of a weakly buoyant plume based on Yoki's correlation. Zukoski, et al., indicated that about 25% of the heat release by combustion is lost from the fire, so the radiation loss was assigned 25% in the model calculation. Furthermore, Zukoski and Kubota computed the theoretical entrianment rate by arbitrarily choosing the value of $\dot{Q}$ in Equation (4.5) to be 70% of the heat release rate based on the fuel flow rate. Zukoski's, et al., flame height measurements are also employed in Figure 14.

In Figure 14 the largest and the smallest fuel flow rates are used in the calculation to bound the experimental data. A porous bed which consisted of glass beads was used as the fire source. Since the initial conditions are not specified and the characteristics of the source are similar to that of McCaffrey [13] and Cox and Chitty [12] refractory burner, source conditions were estimated using the measurements of References 12 and 13.

The entrainment measurements of Zukoski, et al., [14] show that a fire plume entrains proportionately more air, represented by $\dot{m}_p/\dot{m}_{pt}$, near the source, as the source diameter increases. The model agrees with this trend; however, the measurements yield a greater variation with size, over the test range, than is predicted. The values $\alpha_o = 0.182$, $K = 0.1$, provided the best fit of predictions and measurements.

Having fixed the values of α_o and K, the reaction rate constant C_R was determined from the present species concentration data for Flame I. The best fit was obtained using $C_R = 0.17$. The resulting comparison between predictions and measurements is illustrated in Figure 15.

The entrainment constants α_o, K and the reaction rate C_R for the noncombusting fire plumes are summarized in Table 5. With the values of α_o, K and C_R established, the model can be compared with the remaining fire plume measurements.

Similar to the differential model, two limits were examined with respect to radiation. The first limit involved neglecting radiation losses entirely. The second limit involved the assumption that 20% of the total heat of reaction was lost by radiation.

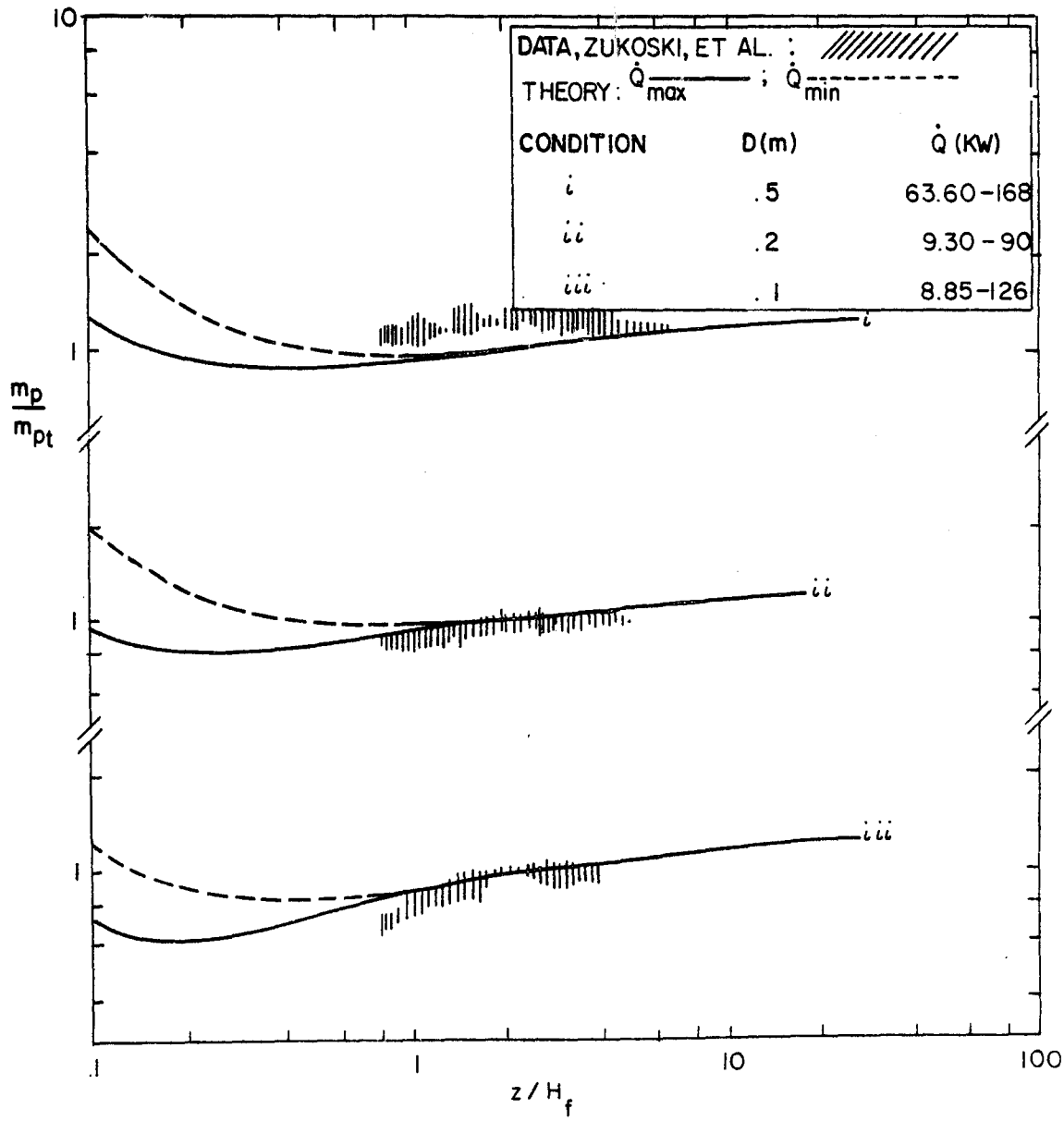

Figure 14. Calibration of the integral model with the data of Zukoski, et al., for strongly buoyant plumes.

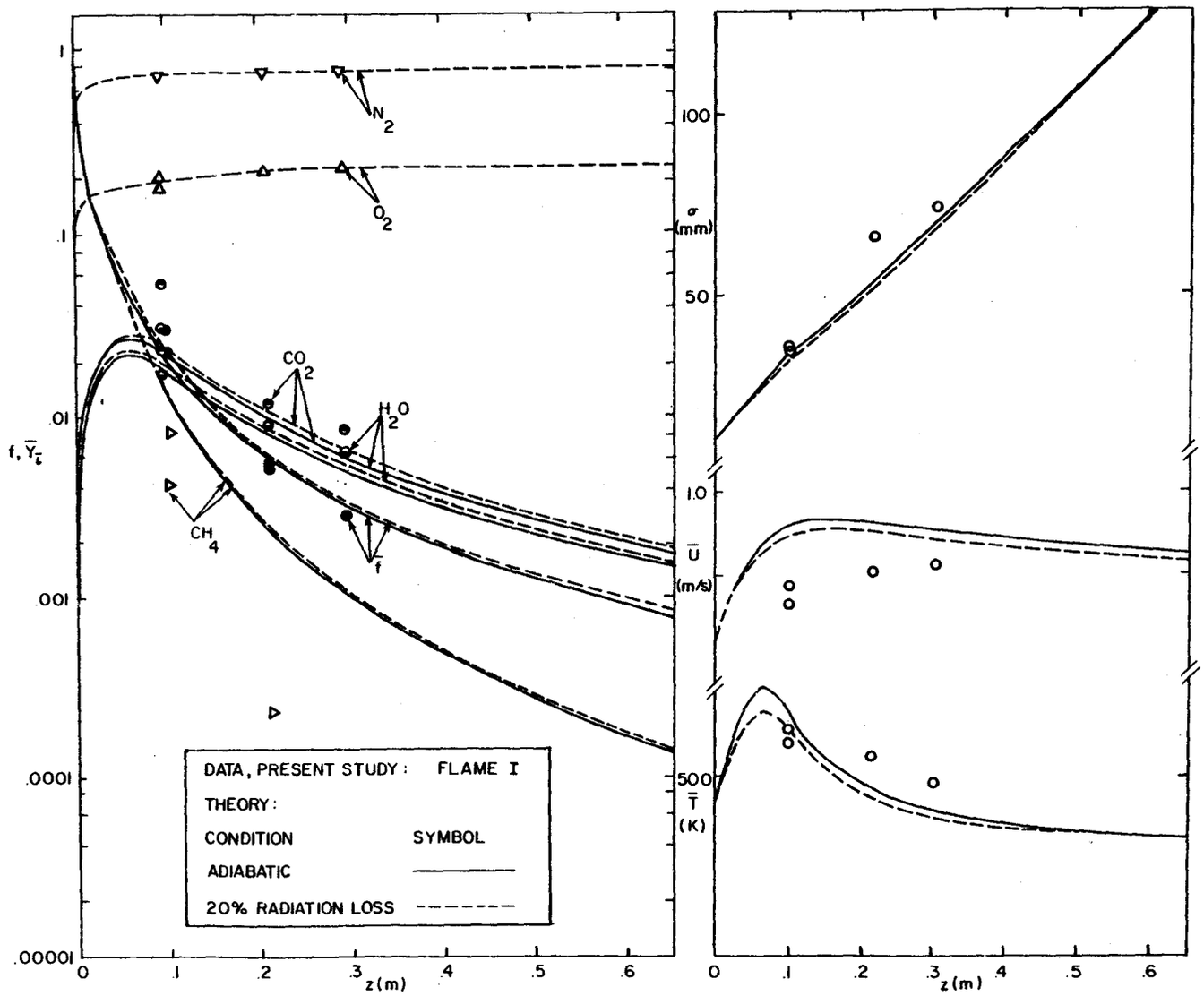

Figure 15. Comparison between the data and the predictions for flame I with the integral model.

Table 5

CONSTANTS FOR THE INTEGRAL MODEL

	α_o	K	C_R
Noncombusting weakly buoyant plume	0.14	0.1	--
Combusting fire plume	0.182	0.1	0.17

Flame I Results

Figure 15 is an illustration of the comparison between the predictions and measurements for Flame I. The variables shown include species concentrations, $\bar{Y}_i$; mixture fraction, $\bar{f}$; plume width, σ; plume velocity, $\bar{u}$ and plume temperature, $\bar{T}$. The measured and predicted species concentrations are in good agreement except for methane. It is believed that the discrepancy in this case is due to experimental error, since methane was present in relatively small quantities. The predicted velocity increases and decays slower than the predicted temperature, since the velocity generated by buoyancy is proportional to the square root of excess temperature in the plume.

The plume width contracts just above the source due to the acceleration of the flow. After a relatively short distance, however, the plume grows once again due to entrainment. When the plume reaches the height of 0.2 meters, the flow begins to decay and the plume grows with nearly constant rate. In general, the theory predicts the plume width reasonably well; however, the model generally overestimates the velocity and tends to underestimate the temperature in the region far from the source. The choice of radiation model appears to have little influence on the results.

Flame II Results

Figure 16 is an illustration of the comparison between predictions and measurements for Flame II. The trends of predictions and measurements are similar to those observed in Flame I. Comparing results for velocity and temperature, we can see that predicted development of flow is faster than measured. It seems that the adopted values of entrainment constants are greater than the appropriate values for Flame II. This can also be seen by the comparison between predicted and the measured mixture fraction f. The prediction underestimates the mixture fraction because the entrainment rate of air is too high in the calculation. In the actual tests, Flame I was less stable than Flame II, therefore, it is not surprising that Flame I entrained more air than Flame II. The results suggest that, an entrainment function, which is directly related to the flow Froude number, may help to improve the predictions of the model.

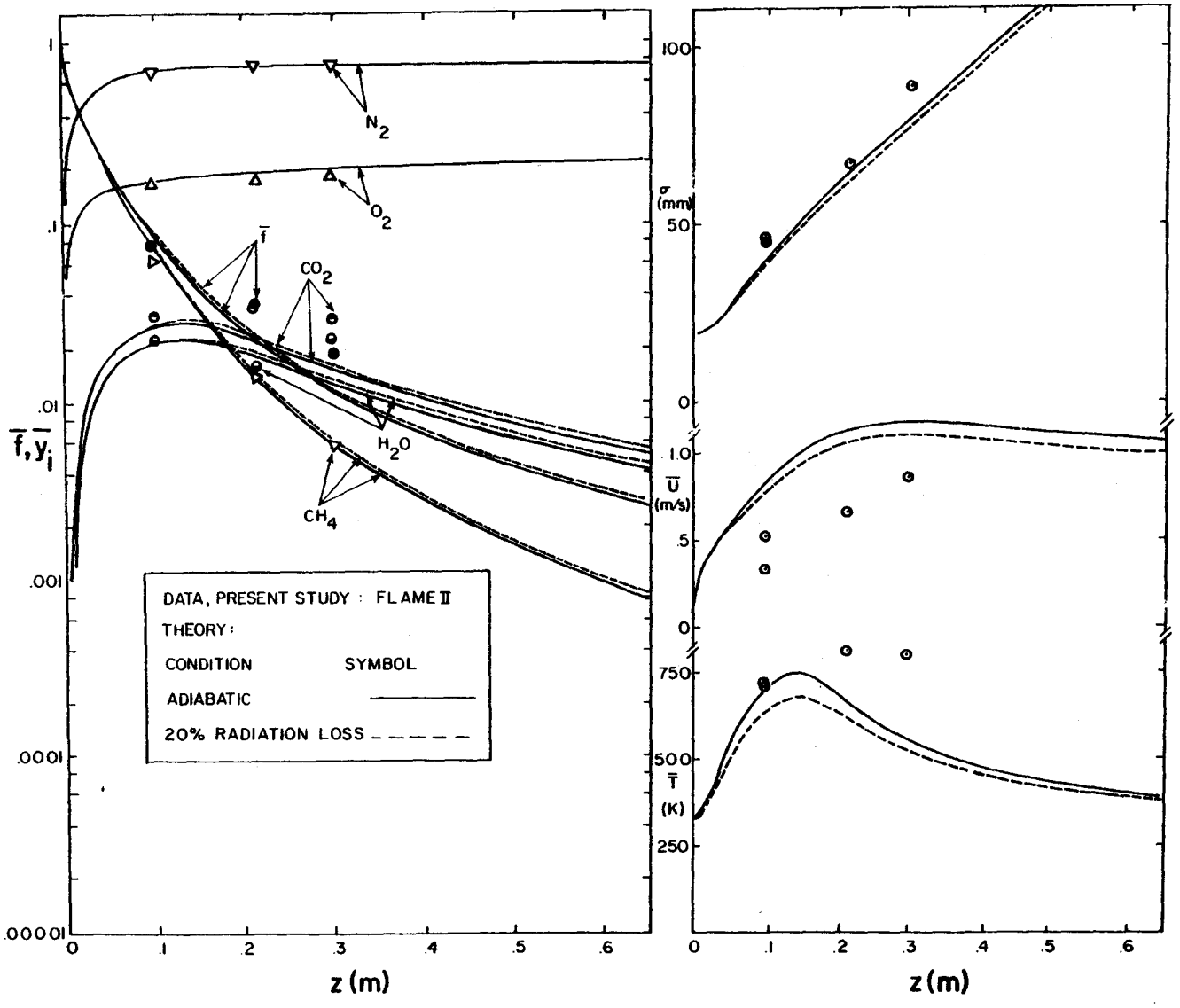

Figure 16. Comparison between the data and the predictions for flame II with the integral model.

Cox and Chitty Results [12]

Figure 17 illustrates the model predictions for the measurements of Cox and Chitty [12]. The initial conditions used in the calculation were obtained by extrapolating the axial measurements of Cox and Chitty to the source. In general, the model predicts the velocity quite well; however, the flow width is underestimated and the temperature is overestimated. Cox and Chitty did not indicate any provisions to reduce disturbances from the surroundings which might be a factor in the large plume widths that were measured. Furthermore, fairly large thermocouples were used during this investigation, tending to make the measured temperatures low, due to radiation errors. This effect could explain some of the error between predictions and measurements--particularly in the high temperature portions of the flow.

McCaffrey Results [13]

Figure 18 shows the comparison between the predictions and the measurements of McCaffrey [13]. Since McCaffrey did not specify his source conditions, the initial conditions for the calculation were obtained by extrapolating his axial measurements. All data reduction employed his proposed correlations. The same trends of predictions and measurements seen with respect to the Cox and Chitty [12] measurements also appear here. The model predicts the velocity quite well, but underestimates the flow width and overestimates the plume temperature. As previously discussed, measured temperatures in high temperature regions are probably low due to radiation losses and the model is probably performing better than indicated in Figure 18. Since McCaffrey correlated his plume-width data into two separate regions, a discontinuity appears in the experimental width correlation illustrated in Figure 18.

Prediction of Plume Radiation

Radiation from fire plumes to surrounding objects is an important aspect of fire modeling. Two approaches were employed to make predictions of this type. In the first method, it was assumed that 20% of the heat of reaction was lost by radiation, similar to the approach used for the flame structure predictions. The rate of heat loss was determined by assuming that the loss occurred as the fuel and oxygen reacted, similar to the approach used by Tamanini [16].

The second model for determining radiation to the surroundings was based on the exponential-wide-band model of Edwards, et al., [31]. This involved considering gaseous radiation from CH_4, CO_2, H_2O and CO, but omitting radiation from soot. Mean species concentrations, temperatures and the flow width were taken as the "top hat" quantities determined from the structure model.

The comparison between the predictions of the two models and the measured radiation to the surroundings from Flames I and II is illustrated in Figure 19. Neither model provides a very satisfactory

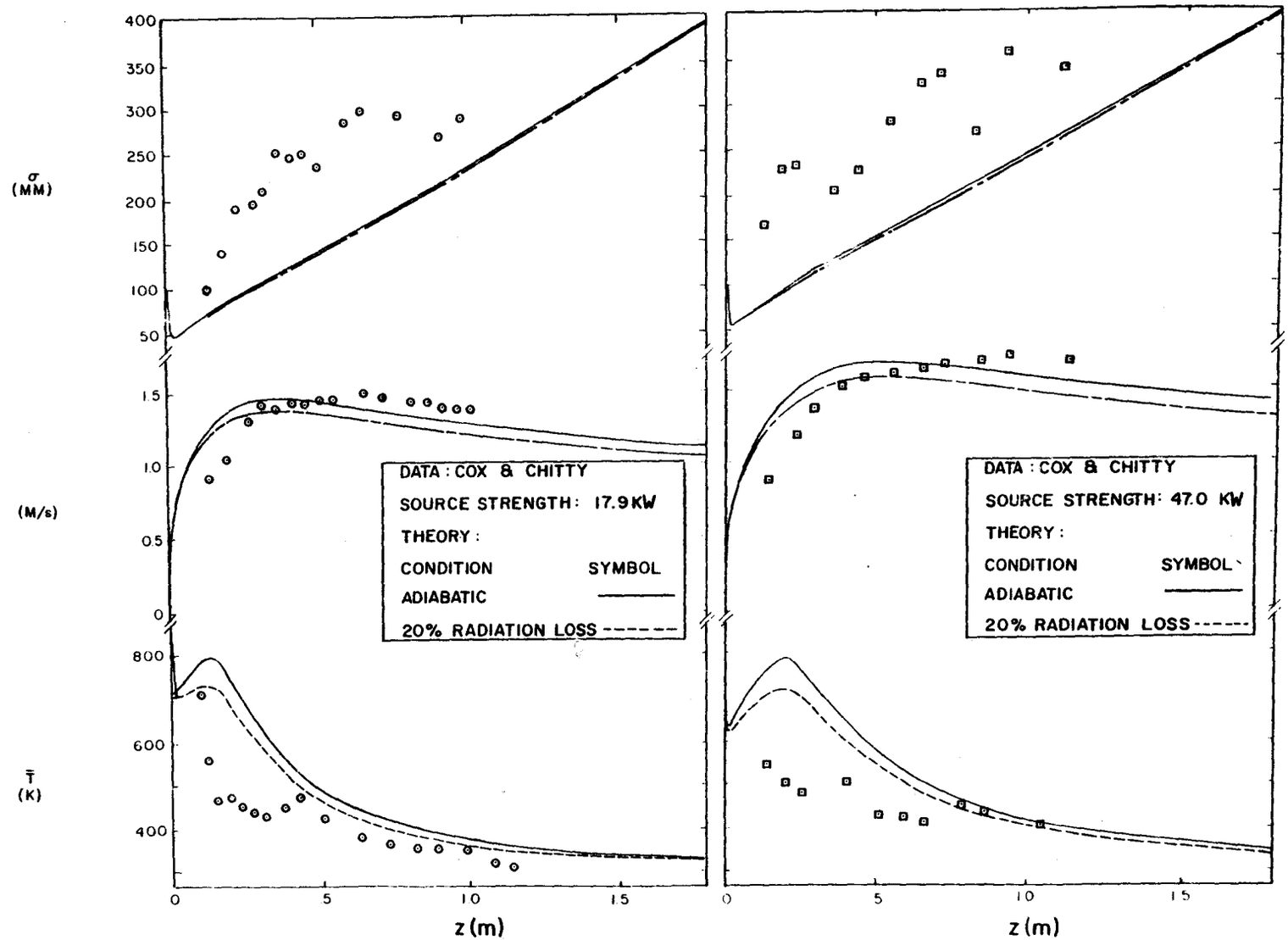

Figure 17. Comparison between the predictions and the data of Cox and Chitty with the integral model.

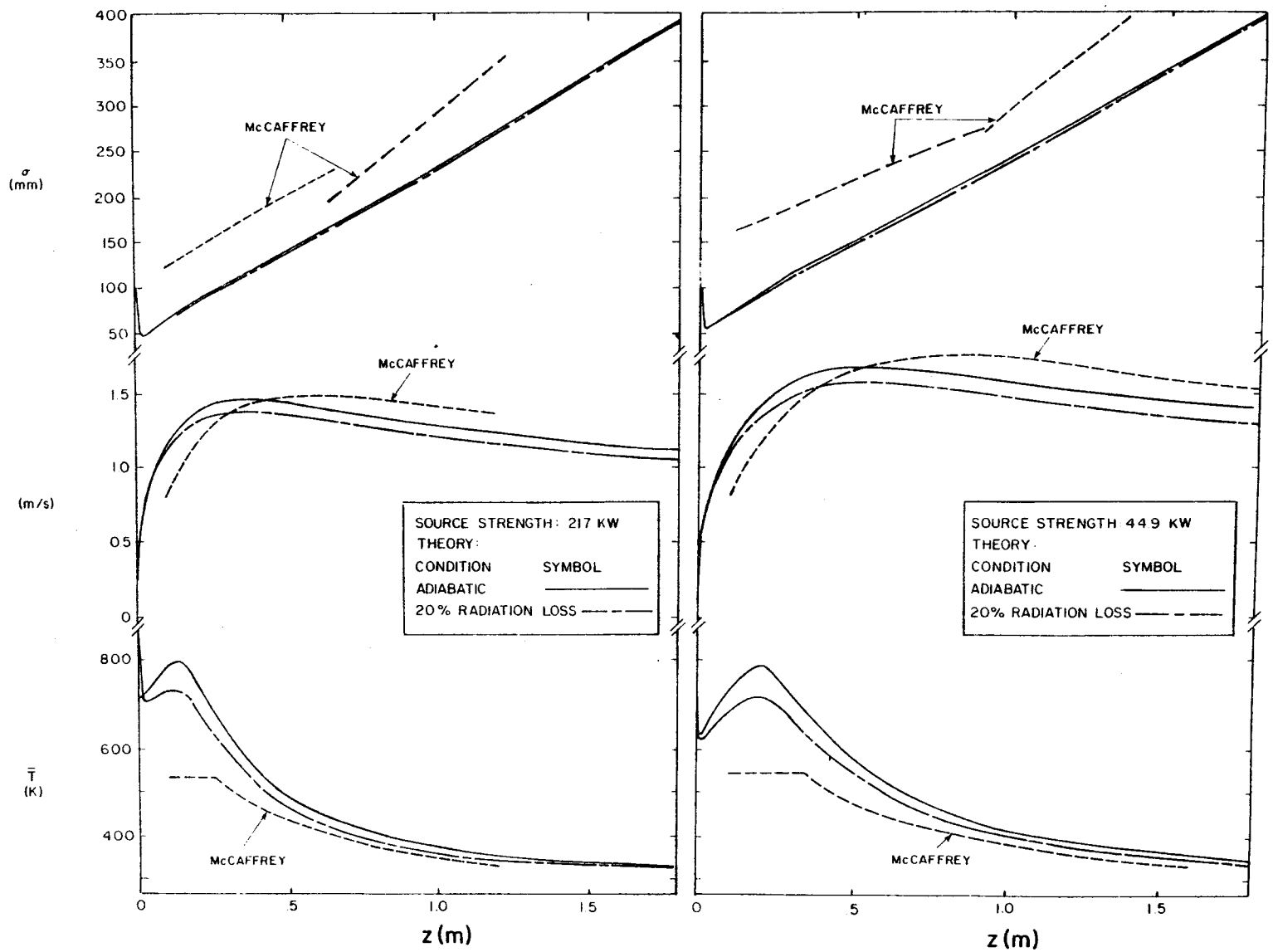

Figure 18. Comparison between the predictions and the data correlation of McCaffrey with the integral model.

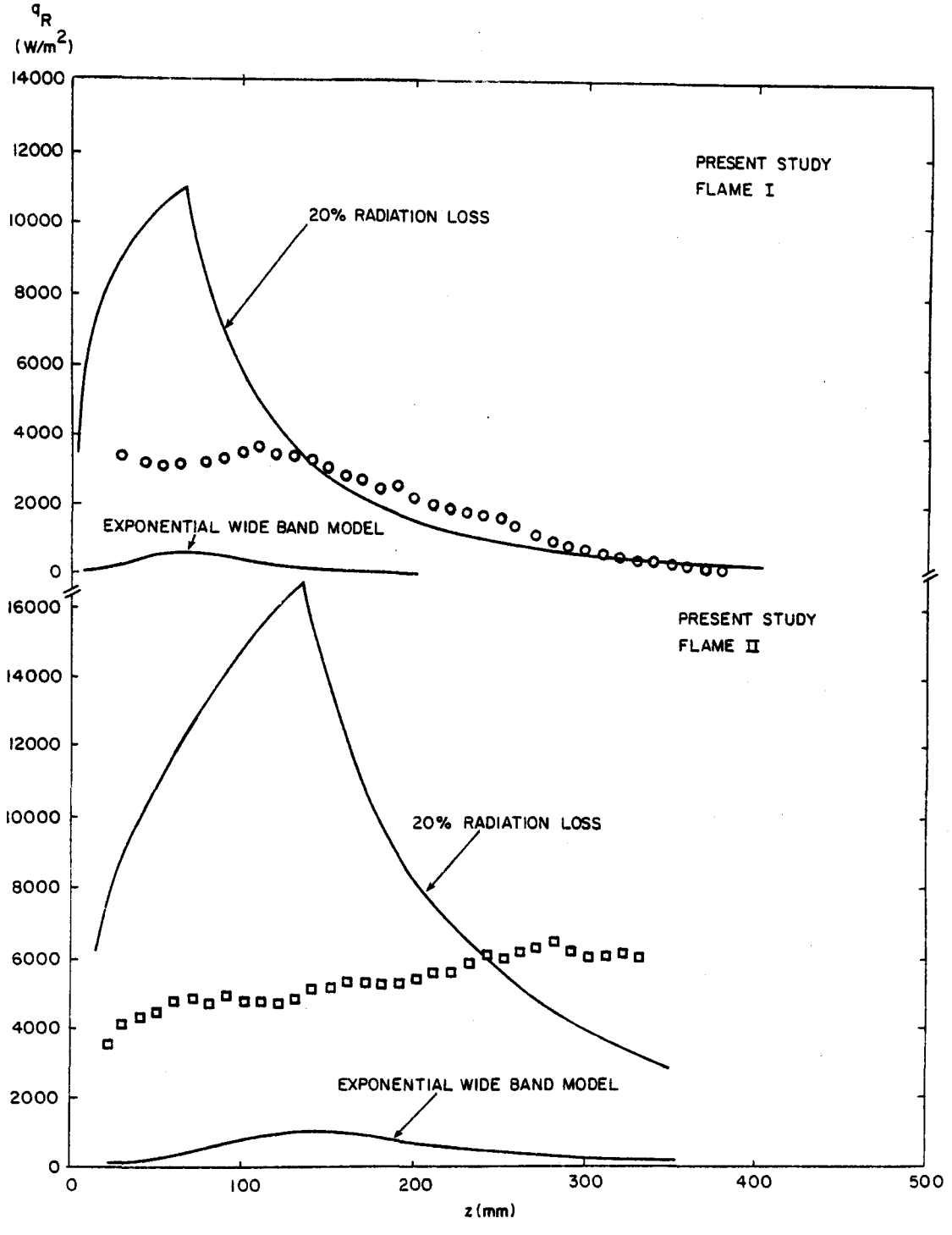

Figure 19. Comparison between the predictions and the data for radiant heat fluxes.

estimation of the measurements. The first method is ad hoc, and there is no physical reason to believe that radiation only occurs when the reaction takes place. The second approach, however, is based on a reasonable representation of radiation physics and the lack of agreement in this case deserves further consideration. The use of "top hat" profiles is one possible reason for the poor agreement. The average temperature is generally less than one-half the maximum temperature in plumes. Use of this temperature would tend to underestimate radiation levels, since radiative power is a nonlinear function of temperature. Similarly, effects of species concentrations on radiation are also nonlinear, introducing uncertainties when concentrations are averaged over a cross-section. Another factor is the effect of soot, which was ignored during the present calculations, but undoubtedly contributes to radiation from the flame.

In order to remedy these problems assumptions of profiles other than "top hat" would have to be introduced. Past work by Wilcox [15] suggests that better predictions of radiant heat fluxes are obtained when this is done; however, some of the simplicity of the present model is lost. Another improvement would involve predicting soot concentrations and the radiation from soot. This last modification could be made within the structure of the present model, but additional measurements are needed to fix model parameters for production and consumption of soot.

5. Theory--Ceiling-Jet Region

5.1 Description of Model

An integral model, which is similar to the model described in Section (3.2), is employed to treat the ceiling-jet region of the flow. In order to be consistent with the treatment of fire plumes, "top hat" profiles are adopted. Except for treating the transverse variation of pressure, the general assumptions employed in the fire plume analysis are also applied to the analysis of ceiling jets. Similar to Section (3.2), other specific assumptions will be introduced as the analysis is developed in the following sections.

5.2 Governing Equations

Since the flow is radially symmetric in the ceiling-jet region, cylindrical coordinates (y, r) are adopted for the analysis; where y is the distance measured vertically downward from the ceiling surface, and r is the radial distance measured from the stagnation point. The velocity components in the y and r directions are u and v, respectively.

Applying the von Karman-Pohlhausen method, neglecting potential and kinetic energies, and utilizing "top hat" profiles, we obtain the following equations [34]:

$$\frac{d}{dr}\,(r\bar{\rho}\bar{v}h) = r\rho_{\infty}\bar{u}_{y=h} \tag{5.1}$$

$$\frac{d}{dr}\,(r\bar{\rho}\bar{v}^2h) = \frac{a}{2}\,r\,\frac{d}{dr}\,[(\bar{\rho} - \rho_\infty)h^2] - \tau_w \tag{5.2}$$

$$\frac{d}{dr}\,[r\bar{\rho}\bar{v}h(\bar{Y}_i - Y_{i\infty})] = rh\bar{P}_i \tag{5.3}$$

$$\frac{d}{dr}\,[r\bar{\rho}\bar{v}h\bar{C}_p(\bar{T} - T_r)]$$

$$= r\rho_\infty\bar{u}_{y=h}C_{p\infty}\,(T_\infty - T_r) - rh_c\,(\bar{T} - T_w)$$

$$+ r\int_0^\infty Q_R dy - rh\sum_i \bar{P}_i h_i^{(o)} \tag{5.4}$$

Similar to Equations (3.17)-(3.20), the quantities on the left-hand side of Equations (5.1)-(5.4) represent the following integrals:

$$B_1 = r\bar{\rho}\bar{v}h = \int_0^\infty vrdy \tag{5.5}$$

$$B_2 = r\bar{\rho}\bar{v}^2h = \int_0^\infty \rho v^2rdy \tag{5.6}$$

$$B_3 = r\bar{\rho}\bar{v}\bar{Y}_ih = \int_0^\infty \rho vY_irdy \tag{5.7}$$

$$B_4 = r\bar{\rho}\bar{v}\bar{C}_p\,(\bar{T} - T_r)h = \int_0^\infty \rho vC_p\,(T - T_r)rdy \tag{5.8}$$

The quantities $\bar{v}$, $\bar{Y}_i$, $\bar{T}$ and h can be calculated from the following relationships:

$$\bar{v} = B_2/B_1 \tag{5.9}$$

$$\bar{Y}_i = B_3/B_1 \tag{5.10}$$

$$\bar{T} = B_4/\bar{C}_p B_1 + T_r \tag{5.11}$$

$$h = B_1/r\bar{\rho}\bar{u} \tag{5.12}$$

where $\bar{\rho}$ can be calculated by knowing the concentrations, $\bar{Y}_i$, and the temperature, $\bar{T}$, using the equation of state for the mixture.

5.3 Parameters in the Governing Equations

Equations (5.1)-(5.4) cannot be solved until appropriate functions for entrained velocity $\bar{u}_{y=h}$, wall shear stress τ_w, production rate of species $\bar{P}_i$, heat transfer coefficient h_c, and radiation loss Q_R are determined.

When the density in the ceiling jet is not much different from the ambient density, Alpert [4] has shown that the entrainment coefficient $\bar{u}_{y=h}/\bar{v}$ is only a function of Richardson number. Based on the entrainment measurements of Ellison and Turner [38] in stratified flows, the entrainment coefficient can be expressed in the following relationship:

$$\bar{u}_{y=h}/\bar{v} = C_c \exp(-\alpha_c Ri) \tag{5.13}$$

where C_c and α_c are constants or functions which must be specified and Ri is the Richardson number, defined as

$$Ri = a(\rho_\infty - \rho)h/\rho_\infty \bar{v}^2 \tag{5.14}$$

If the density defect in the ceiling jet is appreciable, the density effect on entrainment must be considered. For isothermal wall jets, the entrainment constant derived from the velocity measurement of Poreh, et al., []9] are in good agreement with those of free jets [4]. Therefore, as Ri approaches zero, the entrainment constant of ceiling jets can be reasonably assumed to be equal to that of plumes. Referring to Equation (3.31), the entrainment constant in the ceiling jet can be expressed as

$$\bar{u}_{y=h}/\bar{v} = \alpha \exp(-\alpha_c Ri) \tag{5.15}$$

where α is the entrainment function of plumes expressed in Equation (3.31).

Since the flow in the ceiling-jet region is mostly turbulent, parallel to the treatment of reaction rates in the plume region, Equation (3.36) is assumed to be valid in the ceiling flow, except that the plume width, σ, is replaced with the thickness of the ceiling jet, h. Knowing the consumption rate of fuel, Equation (3.37) can again be used to calculate the consumption rate of oxygen and the production rates of carbon-dioxide and water vapor.

The wall shear stress τ_w can be expressed as a function of wall skin friction, f, and flow velocity, $\bar{v}$. In general, the wall shear stress can be expressed as follows:

$$\tau_w = f\bar{\rho}\bar{v}^2/2 \tag{5.16}$$

For the present flow condition, we can use the Reynolds' analogy to relate wall shear stress to wall heat flux. From this analogy, the heat transfer coefficient, h_c, is proportional to wall skin friction,

$$h_c/\bar{\rho}\bar{v}\bar{C}_p = f\ Pr^{-2/3}/2 \tag{5.17}$$

where Pr is the Prandtl number of the mixture.

In the ceiling-jet region, the ceiling also plays a role in radiation heat transfer. Assuming a constant fraction of radiation loss from the flow, similar to plume region, may not apply in the ceiling flow. Therefore, only the exponential-wide-band model [31] was employed to evaluate the radiation loss. Assuming that the flow is optically thick in the radial direction, we have the following expression for radiation loss from the ceiling flow, [34]:

$$\int_0^\infty Q_R dy = \sum_{k=1}^{K} \pi D_k S g_k [2\ I_{b,k}(\bar{T}) - I_{b,k}(T_w) - I_{b,k}(\bar{T}_e)] \tag{5.18}$$

5.4 Computations

The initial conditions required to integrate Equations (5.1)-(5.4) are provided by directly measuring the flow properties at the starting position of the ceiling jet. If measurements of initial conditions are not available, assumptions must be made to relate the properties in the ceiling jet to those in the impinging plumes, as described in the following.

For impinging weakly buoyant plumes, Alpert [4] obtained the initial conditions of ceiling jets using the properties of plumes. He assumed that mass and energy in the flow are conserved in the impingement

region, and that the velocity profiles at the onset of ceiling jets are Gaussian with their maximum velocities being equal to the maximum velocities of impinging plumes. The initial conditions of ceiling jets for "top hat" profiles are then as follows [4]:

$$z_o = H(1 + 3\,\alpha_o/5\gamma)^{-1} \tag{5.19}$$

$$h_e = \sqrt{2}\,\sigma_o^{\,2}/2r_e \tag{5.20}$$

$$\bar{v}_e = \bar{u}_{c,o}/\sqrt{2} \tag{5.21}$$

$$\bar{\rho}_e = \rho_\infty - \beta^2(\rho_\infty - \bar{\rho}_{c,o})/(1 + \beta^2) \tag{5.22}$$

where r_e is the starting position of the ceiling jets, which corresponds to the edge of impinging plumes where $\bar{u}/\bar{u}_{c,o} = 0.05$. Other quantities are defined in the Nomenclature.

The integration method used in the plume region was also employed in the ceiling-jet region.

6. Results and Discussion--Ceiling-Jet Region

6.1 Predicted and Measured Flow Structure

Two new model constants have to be assigned to complete calculations in ceiling jets. These two constants are α_c, which regulates the effect of Richardson number on entrainment, and f, the skin fraction factor of the ceiling.

Based on the entrainment measurements of Ellison and Turner [38] in stratified layers, the value of α_c is around 5. Ellison and Turner undertook their experiments by issuing lighter or heavier liquids into a channel-like reservoir. To reduce disturbance in the upstream region, they let buoyancy-inducing liquids flow parallel to the solid boundary and then into the channel. For the present impinging plumes and flames, the suppression effect of buoyancy on entrainment in ceiling jets is reduced due to the substantial disturbance of the impingement region. This implies that the appropriate value of α_c for present flows should be less than 5.

A correlation of skin friction factor for present ceiling flows cannot be found in the literature. According to the Blasius equation and the friction correlation of Poreh, et al., for wall jets induced by isothermal impinging turbulent jets [39], the friction factor is only weakly dependent on the Reynolds number. Furthermore, the present data show that the ceiling-jet thickness grows while velocity decays when the flow moves away from the impingement region. Therefore, the Reynolds number tends to vary moderately in the ceiling-jet region. Without precise information on skin friction, it is reasonable to assume a constant friction factor for ceiling-jet flow.

The optimum values of α_o, α_c and f are found to be 0.182, 1.5 and 0.025 respectively, in order to match the measurements of ceiling heat transfer and flow thickness of Flame I. Other model constants of ceiling jets are taken from their corresponding results in the plume region.

Flame I Results

Figure 20 is an illustration of the comparison between the predictions and the measurements of Flame I in the ceiling-jet region. The variables shown include species concentrations, $\bar{Y}_i$; mixture fraction, $\bar{f}$; ceiling-jet thickness, h; ceiling-jet velocity, $\bar{v}$; and ceiling-jet temperature, $\bar{T}$. Complete profiles of mean temperature and mean velocity were taken at five radial positions, while profiles of species concentrations were measured at three radial locations. Since the species concentrations vary moderately in ceiling-jet region, the species concentrations of those locations where data were not taken were interpolated or extrapolated from the measurements at neighboring locations, in order to transform the profiles of temperature and velocity into "top hat" quantities. The initial conditions in the calculation are directly taken from the measurements at r = 76 mm.

The predicted and the measured species concentrations are in good agreement except for water vapor. The theory underestimates the water vapor in the downstream region. This discrepancy is thought to be due to moisture condensed on the ceiling, as well as ambient humidity levels. These factors would tend to yield the measured concentrations of water vapor which are relatively constant along the ceiling.

The flow contracts near an r/H of 0.3. Alpert [4] observed a contraction point near r/H = 0.2 for weakly buoyant impinging plumes. We have already seen that Flame I has a higher entrainment constant and hence a greater plume width than comparable weakly buoyant plumes. Therefore, it is not surprising that the starting point of the ceiling jet of Flame I is farther from the stagnation point. Near the edge of the ceiling (r = 500 mm), the flow thickness drops because of flow acceleration. In general, predicted and measured temperatures and velocities are in good agreement.

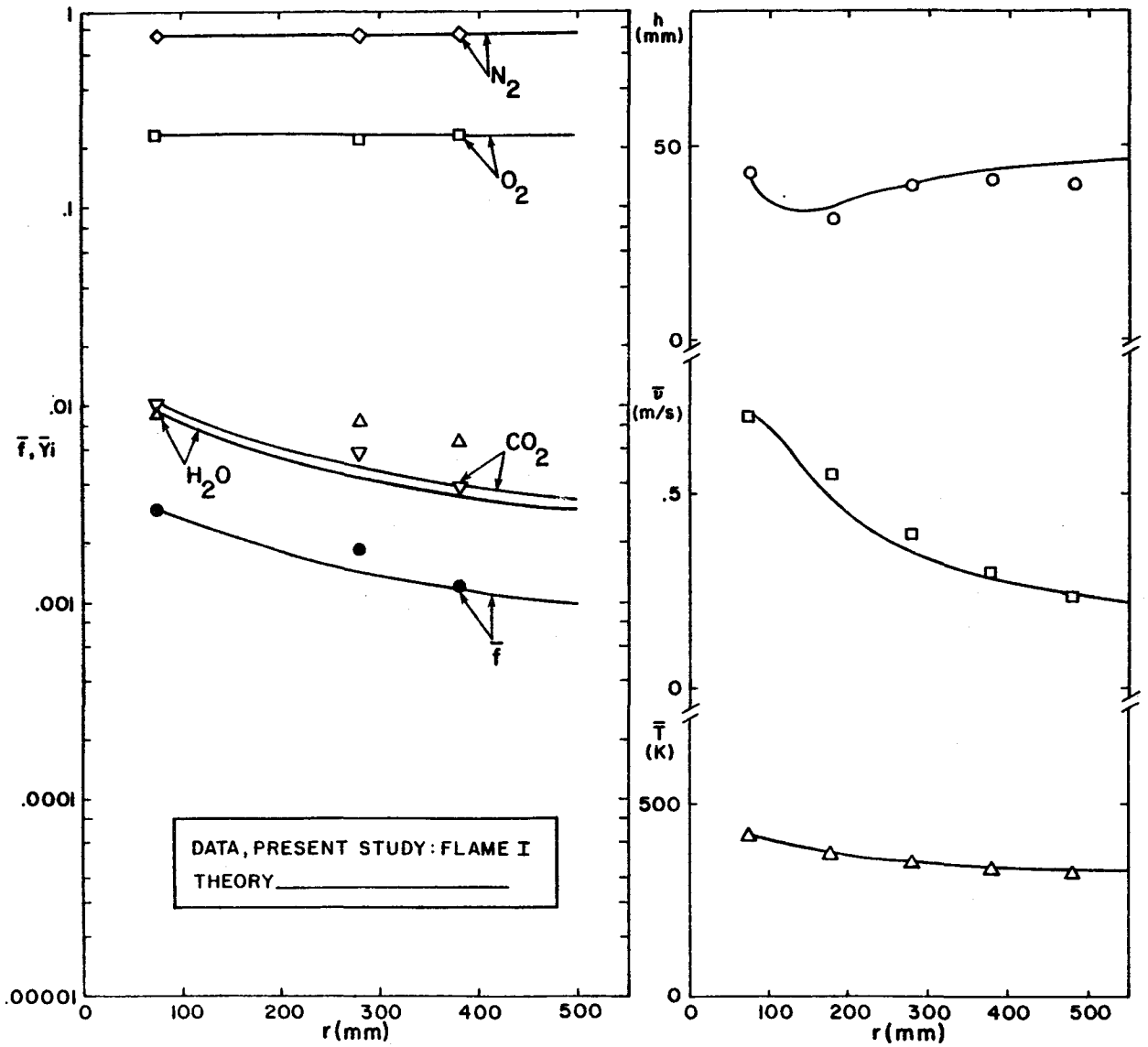

Figure 20. Comparison between the data and the predictions of the integral model in the ceiling-jet region of flame I.

Flame II Results

Figure 21 is an illustration of the comparison between the predictions and the measurements for Flame II. For Flame II the flame tip can sometimes reach 300 mm radially from the stagnation point. Similar to Flame I, the measured concentration of water vapor only varies moderately with radius and the model underestimates its value near the edge of the ceiling. Except at the initial position, the amount of methane present in the ceiling jet is too small to be detected.

Similar to Flame I, the flow contracts at $r/h \approx 0.3$ and the thickness is reduced again near the edge of the ceiling, due to flow acceleration. The model somewhat underestimates flow velocity and overestimates flow velocity and overestimates flow temperature. Overall, fair agreement still exists between the predictions and the measurements.

Ceiling-Jet Results of Alpert [4]

Figure 22 shows the comparison between the present predictions and Alpert's measurements [4] in ceiling jets resulting from weakly buoyant plumes. The flow properties considered are flow thickness, h; velocity, $\bar{v}$; and temperature, $\bar{T}$. In order to facilitate the comparison for different heat sources, flow properties are normalized with appropriate parameters proposed by Heskestad [40], which can correlate the predictions for various heat sources into a single curve.

Model constants employed for Flame I and Flame II have to be modified for weakly buoyant plumes. As discussed earlier, the value of entrainment constant α_o is equal to 0.14 for weakly buoyant flows. Due to the lack of detailed information on Alpert's test conditions, the values of α_o and α_c were chosen to be 0.14 and 1.5 in order to be consistent with the previous findings. Since Alpert bounded his heat transfer data with f - 0.02 and 0.04 [4], and since the variation of flow thickness, velocity and temperature is not very sensitive to the value of f, the value of f - 0.03 was chosen for the computations. The initial conditions in the calculation were specified by the fire strength and the ceiling height, utilizing Equations (5.19)-(5.22) and correlations for weakly buoyant plumes [6].

Overall, the present model provides a fair prediction of the flow properties of Alpert's ceiling jets. The underestimation of flow thickness may be due to ambient disturbances in Alpert's test environment, similar to the earlier results for plumes. Therefore, a larger value of α_o or a smaller value of α_c is needed to correctly predict Alpert's flow width. In order to maintain the essence of a model prediction, however, the values of α_o and α_c were not changed.

The initial values of measured and predicted temperatures imply that the center-line temperatures of Alpert's impinging plumes are lower than the temperature correlation of Rouse, et al., [6] and the present study, which is employed to provide the initial value of ceiling-jet temperature.

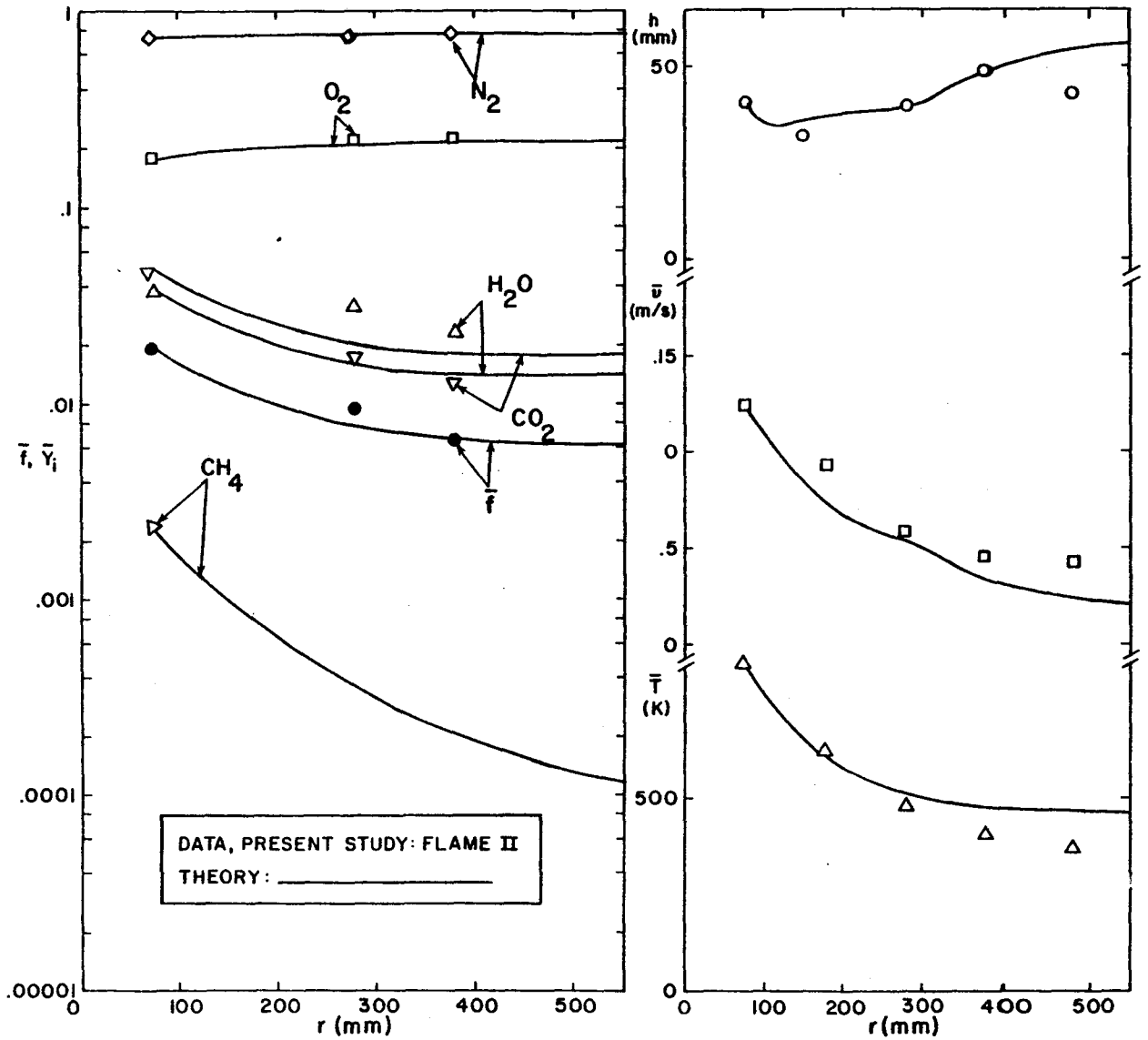

Figure 21. Comparison between the data and the predictions of the integral model in the ceiling-jet region of flame II.

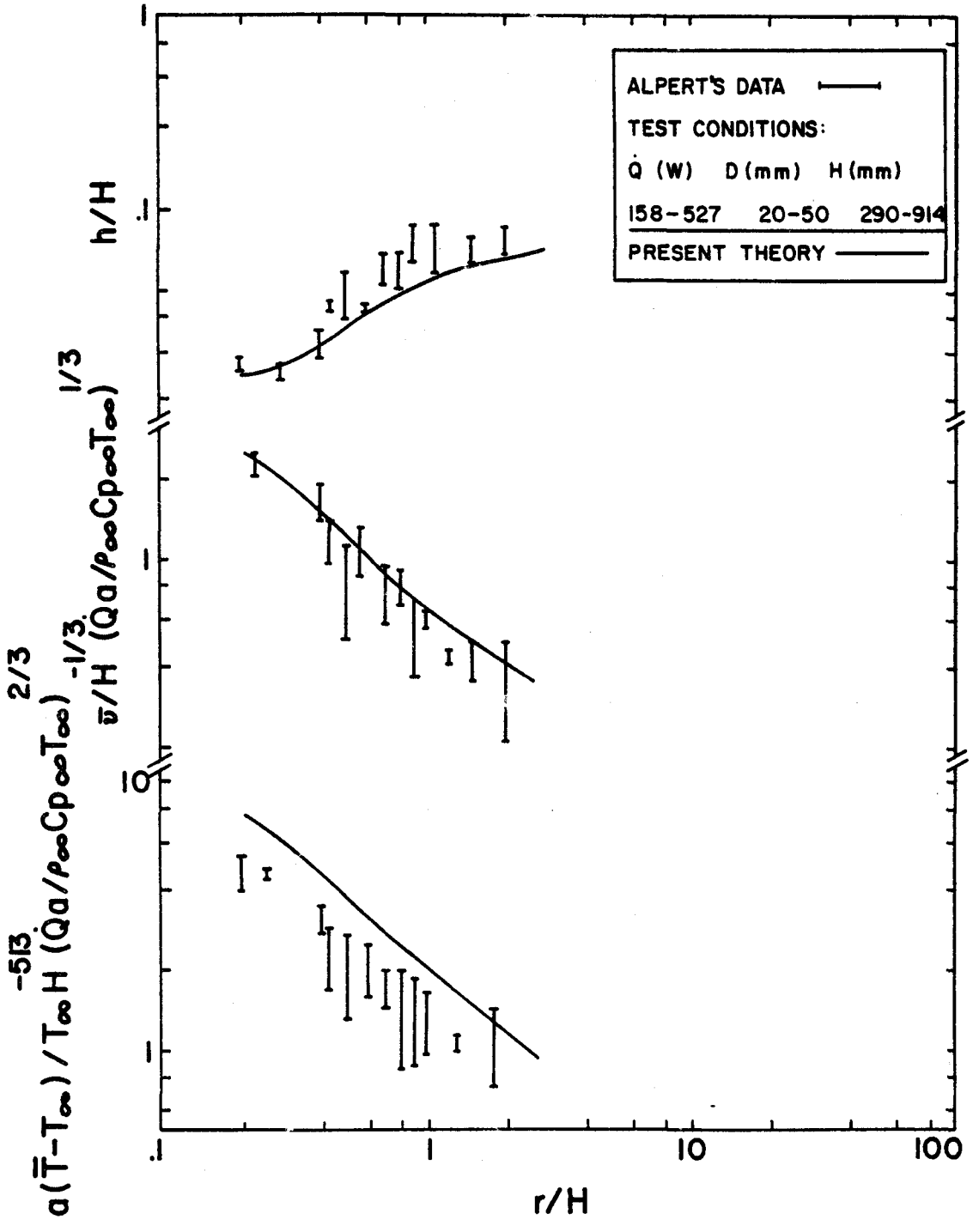

Figure 22. Comparison between the predictions of the integral model and the data of Alpert in ceiling-jet region.

6.2 Predicted and Measured Heat Transfer Rates

Figure 23 is an illustration of the variation of ceiling heat flux with radial distance from the stagnation point. These results are for unconfined ceilings. In addition to data taken from the present transient apparatus, measurements are also included from the work of Alpert [4] and Zukoski, et al., [5].

Two sets of predictions for ceiling jets are presented; one from Alpert's numerical solution with $\alpha_c = 5$, the other is the present model prediction with $\alpha_c = 1.5$. The data in the impingement region are bounded with the stagnation-point theory, using two values of Rayleigh number. In initial conditions are found using the same procedure described in the preceding section.

The scatter of the data on Figure 23 is appreciable. Clearly not all relevant factors are considered by these simple correlation schemes. Alpert [4] employed f = 0.02 and 0.04 to bound most of his measurements. With the value of α_c equal to 1.5, the present model generally underestimates the measurements of Alpert [4] and the present study; however, the predictions do bound the data for Zukoski, et al., [5]. If $\alpha_c = 5$ is employed, the predictions of the present model will be close to Alpert's predictions but somewhat lower. However, the increase of α_c would result in poorer predictions of flow properties in Figure 22.

Because of the uncertainty of α_c, it is hard to tell whether the discrepancy in the downstream region is due to the theory or to measurement errors caused by lateral heat conduction through the ceiling. Further study of the entrainment of stratified layers and more heat flux measurements are needed to resolve the uncertainty.

Figure 24 is an illustration of the radial variation of convective ceiling heat flux for the present measurements. The measurements are taken from both the strongly buoyant fire plumes, Flame I and Flame II, and from the weakly buoyant plumes generated by a Bunsen burner. To be consistent with the findings in plumes and ceiling jets in the model calculation, the value of α_c is chosen 1.5 while the value of α_o is 0.182 for strong plumes and 0.14 for weak plumes. The initial conditions of Flame I and Flame II are directly taken from the measurements at r = 76 mm; however, the initial conditions of weak plumes are provided by the scheme Alpert proposed to relate ceiling jets to impinging plumes [4].

In the impingement region, ceiling heat flux decreases as the ratio of flame height to ceiling height increases. In the ceiling-jet region, the effect of flame impingement on heat transfer rate is reduced for weak plumes, but the effect is still appreciable for strong fires. Apparently, the present parameter cannot completely correlate the data taken from a wide range of fire sources.

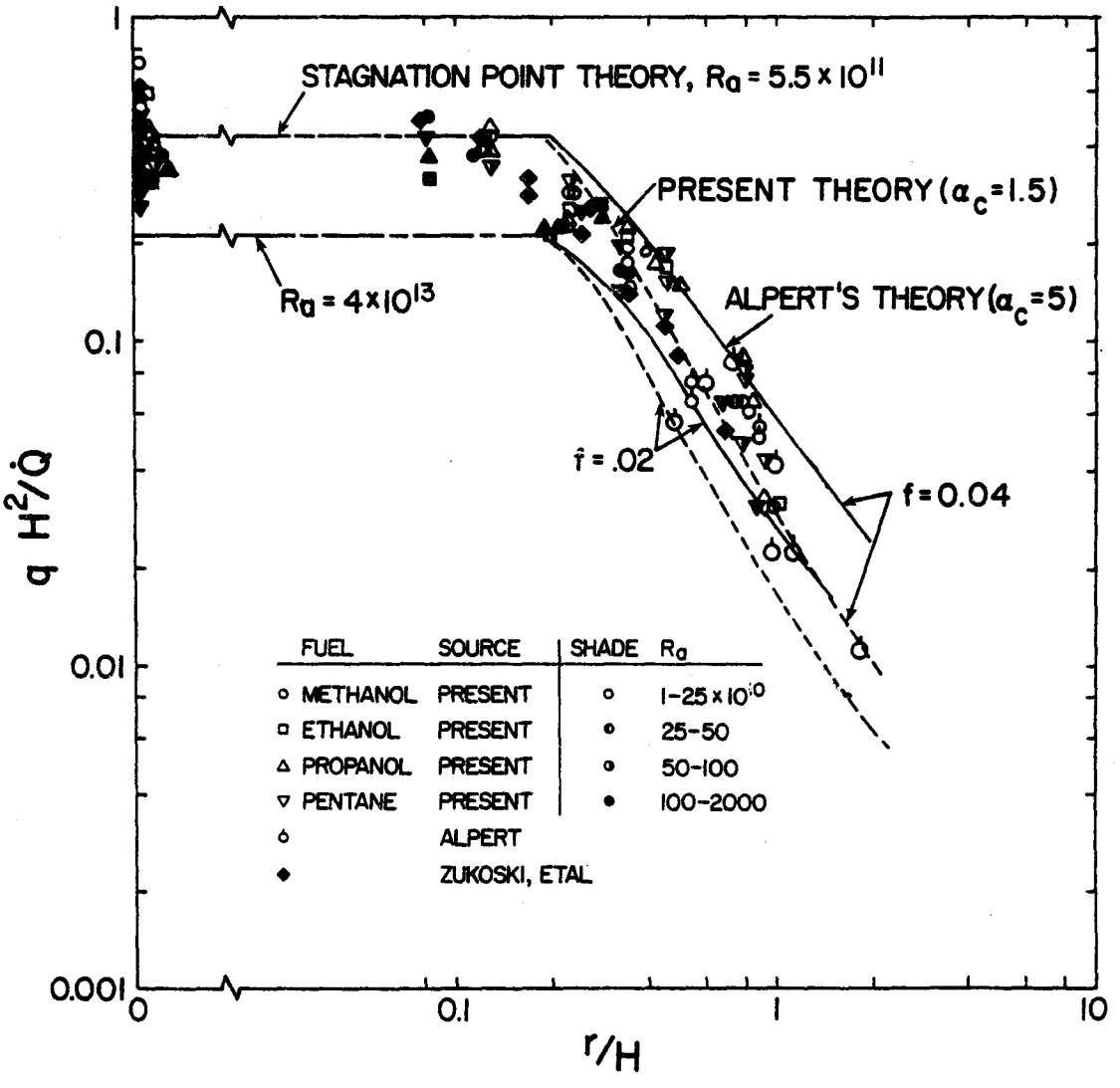

Figure 23. Ceiling heat fluxes for plume impingement on an unconfined ceiling.

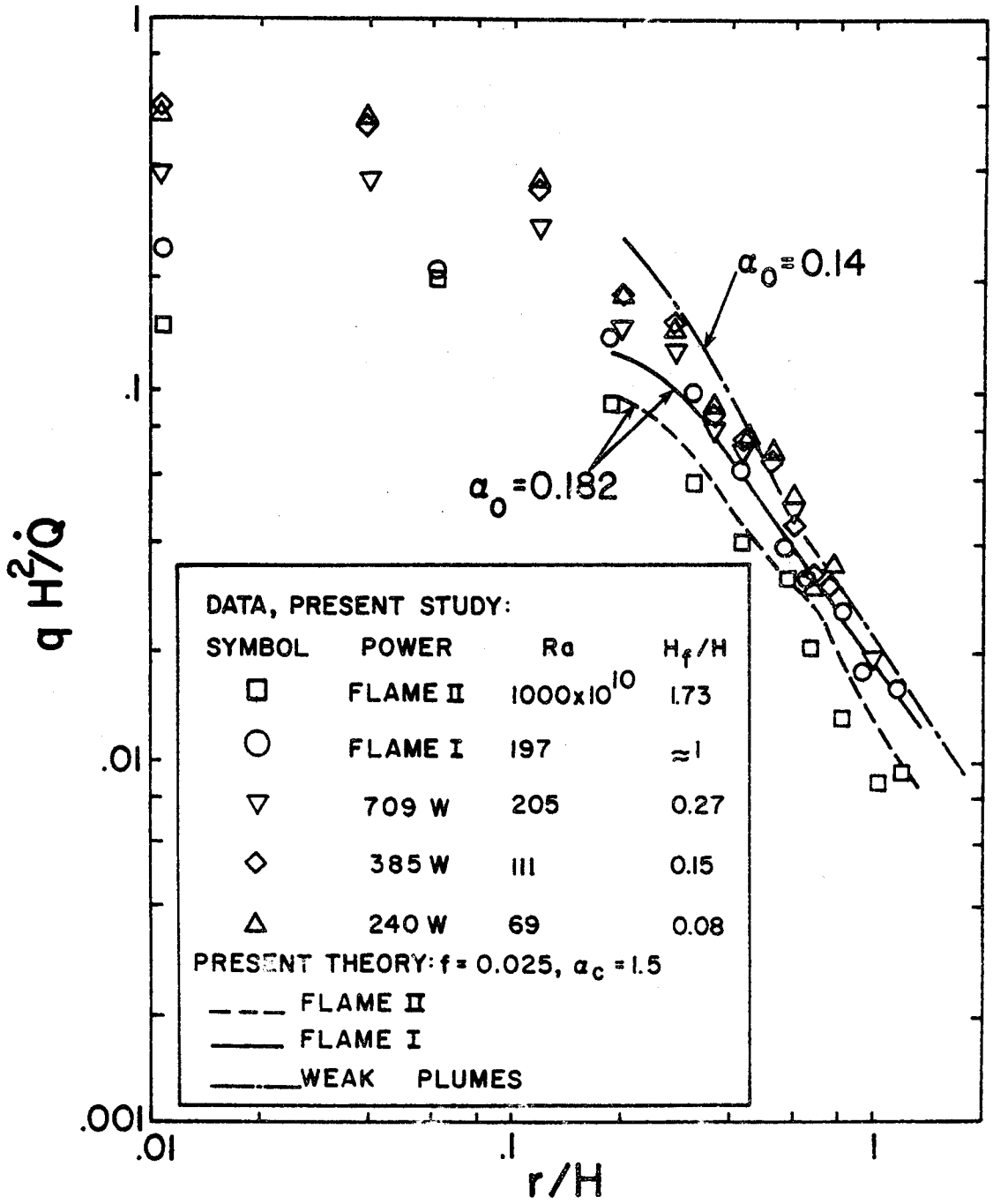

Figure 24. Convective ceiling heat fluxes for plume or fire impingement on an unconfined ceiling using the steady-state apparatus.

The predictions of the present model for Flame I, Flame II and weakly impinging plumes are also illustrated in Figure 24. Overall, the predicted and the measured values are in very good agreement.

Figure 25 is a replot of the data, using the stagnation point heat flux parameter for the abscissa. This choice nicely collapses all the results in the ceiling-jet region to a single line. In fact, the scatter is greatest in the stagnation region, where flow development and incomplete combustion effects exert the greatest influence. If the branch region $0.04 < r/H < .3$ is approximated by the straight line segments illustrated in Figure 25, the following correlation is obtained for the ceiling heat flux of the steady-state apparatus.

$$(qH^2/\dot{Q})Ra^{1/6}\ Pr^{3/5} = 31.2 \quad , \quad r/H < 0.16$$

$$= 1.46(r/H)^{-1.63} \quad , \quad r/H > 0.16 \qquad (6.1)$$

for the range $10^9 < Ra < 10^{14}$, $H_f/H < 1.7$, $Pr \simeq 0.7$. Equation (6.1) only includes convection; any additional contribution due to radiation must be computed separately.

6.3 Effect of Radiation on Heat Flux

For Flame I, the measured ceiling heat flux contributed by radiation is about 15% of the convective heat flux in the impingement region and there is no radiation contribution near the ceiling edge [34]. For Flame II, the radiation heat flux is as much as 35% of the convective value in the impingement region and around 10% near the ceiling edge. On the other hand, the predicted radiation flux of Flame I is around 8% and 3% in the impingement region and at the ceiling edge, respectively, as fractions of the convective heat fluxes. For Flame II, the predicted values of radiation heat flux are much higher than the measurements, 53% in the impingement region and 33% near the ceiling edge. Since the flame tip of Flame II can reach halfway across the ceiling, the inevitable tarnishing of gold foils on the heat flux gauges tends to make the apparent convective heat fluxes greater than their real values, and in this manner lowers the apparent radiation heat fluxes.

Figure 26 shows the comparison between the predictions and the measurements of radiant heat flux to the surroundings for Flame II along the ceiling. The model gives right trend of the measurements; however, the theory underestimates the radiation near the impingement region and overestimates the radiation near the ceiling edge. Because the present radiometer has a relatively large viewing angle (150°), the measured radiant fluxes from the hot fire plumes tend to bias the measurements near the impingement region to higher values. In the region near the ceiling edge, there is no net radiation contribution from the ambience to the radiometer. Since the model evaluates radiation based on local temperatures of the ceiling jets, the predicted value tends to be greater than the measurements near the ceiling edge.

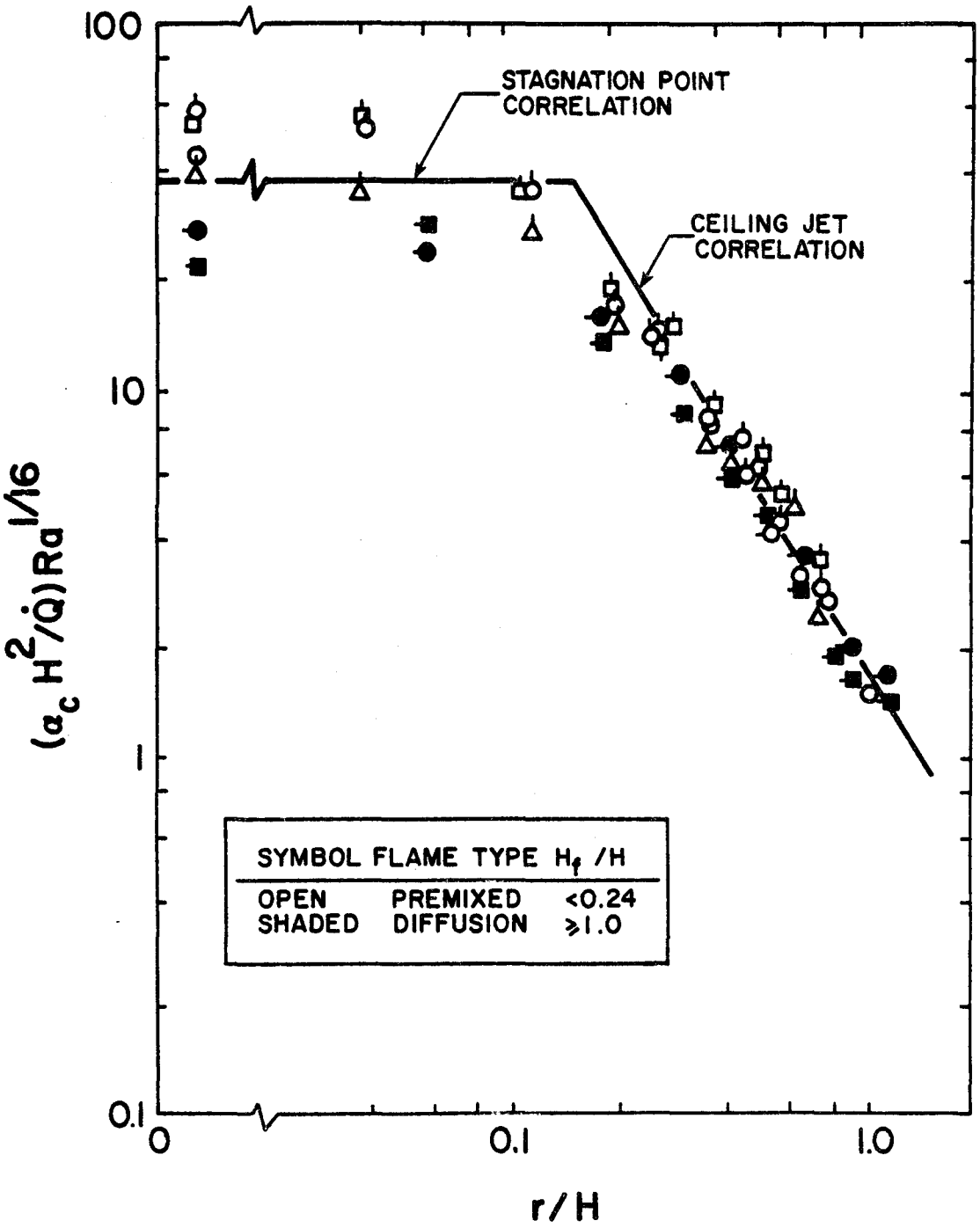

Figure 25. Replot of figure 24.

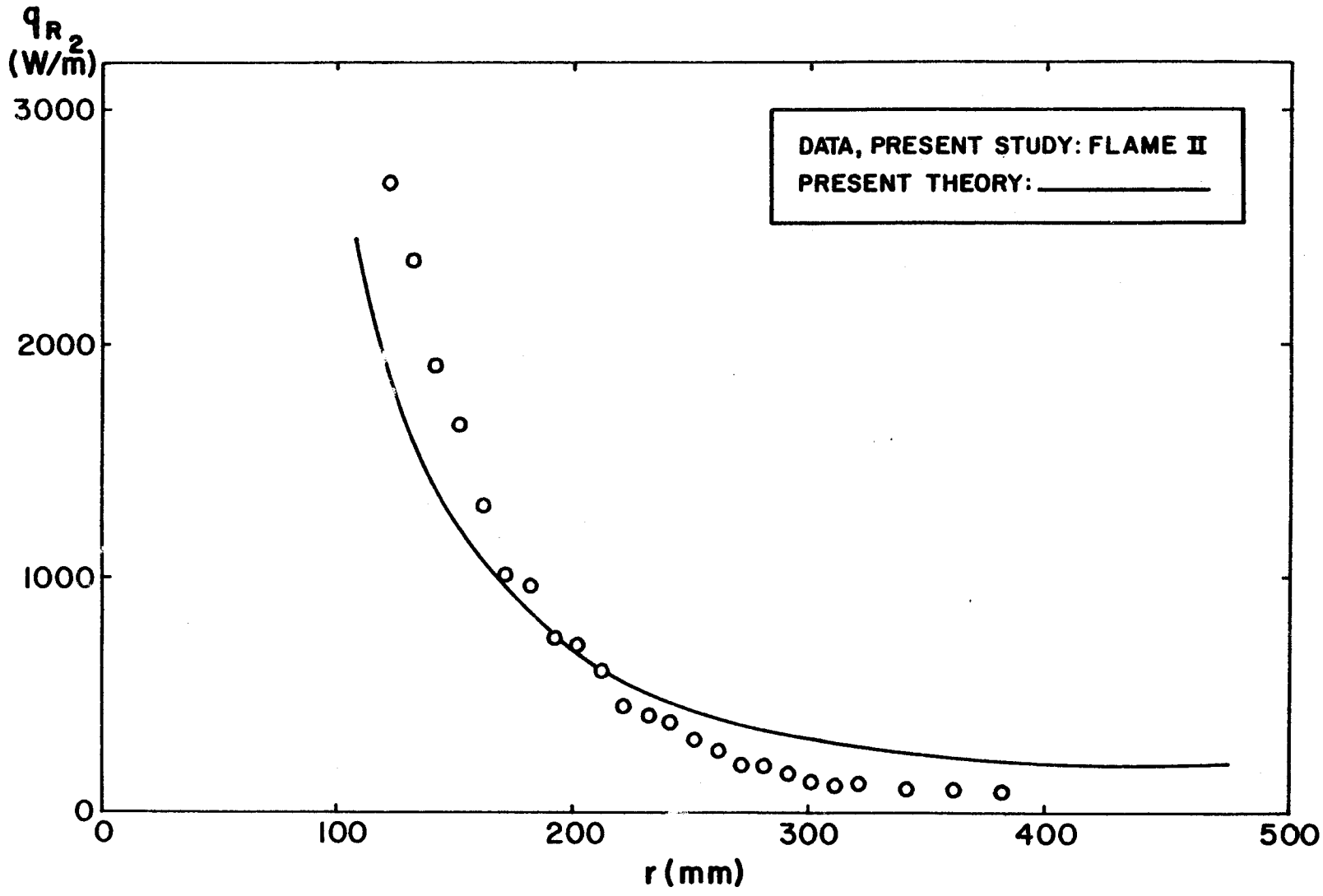

Figure 26. Radiant heat fluxes to the surroundings for flame II in the ceiling-jet region.

References

1. You, H-Z. and Faeth, G. M., "An Investigation of Fire Impingement on a Horizontal Ceiling," Report under USDC-NBS Center for Fire Research, Grant No. 7-9020, October 1978.

2. Ibid., October 1979.

3. Alpert, R. L., "Fire Induced Turbulent Ceiling Jet," Technical Report No. 19722-2, Factory Mutual Research Corporation, Norwood, MA, 1971.

4. Alpert, R. L., "Turbulent Ceiling Jet Induced by Large-Scale Fire," Technical Report No. 22357-2, Factory Mutual Research Corporation, Norwood, MA, 1974.

5. Zukoski, E. E., Kubota, T. and Veldman, C. C., "Experimental Study of Environment and Heat Transfer in a Room Fire," Technical Report No. 1, Grant No. 5-9004, California Institute of Technology, Pasadena, CA, 1975.

6. Rouse, H., Yih, C. S. and Humphreys, H. W., "Gravitational Convection from a Boundary Source," Tellus, Vol. 4, pp. 201-210, 1952.

7. Yih, C. S., "Free Convection Due to Boundary Sources," Fluid Models in Geophysics, Proceedings of the First Symposium on the Use of Models in Geophysical Fluid Dynamics, Johns-Hopkins University, pp. 117-133, September 1-4, 1953.

8. Yokoi, S., "Upward Convection Current From a Burning Wooden House," International Symposium on the Use of Models in Fire Research, Publication 786, National Academy of Science--National Research Council, Washington, DC, pp. 186-206, 1961.

9. George, W. K., Jr., Alpert, R. L. and Tamanini, F., "Turbulence Measurements in an Axisymmetric Buoyant Plume," Technical Report No. 22359-2, Factory Mutual Research Corporation, Norwood, MA, 1976.

10. Chen, C. J. and Rodi, W., "On Decay of Vertical Buoyant Jets in Uniform Environment," Sixth International Heat Transfer Conference, Toronto, Ontario, Candad, August 7-11, 1978.

11. Chen, C. J., and Chen, C. H., "On Prediction and Unified Correlation for Decay of Vertical Buoyant Jets," ASME Paper No. 78-HT-21, 1978.

12. Cox, G. and Chitty, R., "A Study of the Deterministic Properties of Unburned Fire Plumes," Building Research Establishment, Fire Research Station, Borehamwood, WD6 2BL, United Kingdom, 1979.

13. McCaffrey, B. J., "Purely Buoyant Diffusion Flames: Some Experimental Results," Center for Fire Research, National Engineering Laboratory, National Bureau of Standards, Report No. NBSIR 79-1910, 1979.

14. Zukoski, E. E., Kubota, T. and Cetegen, B., "Entrainment in the Fire Plume," Technical Report, Grant No. G8-9014, California Institute of Technology, Pasadena, CA, 1980.

15. Wilcox, D. C., "Model for Fires with Low Initial Momentum and Nongray Thermal Radiation," AIAAJ, Vol. 13, pp. 381-386, March, 1975.

16. Tamanini, F., "An Integral Model of Turbulent Fire Plumes," Technical Report No. RC80-BT-12, Factory Mutual Research Corporation, Norwood, MA, 1980.

17. Tamanini, F., "Reaction Rates, Air Entrainment and Radiation in Turbulent Fire Plumes," Combustion and Flame, Vol. 30, pp. 85-101, 1977.

18. Tamanini, F., "The Effect of Buoyancy on the Turbulence Structure of Vertical Round Jets," J. Heat Transfer, Vol. 100, pp. 659-664, 1978.

19. You, H-Z. and Faeth, G. M., "Ceiling Heat Transfer During Fire Plume and Fire Impingement," J. of Fire and Materials, Vol. 3, pp. 140-147, 1979.

20. Lockwood, F. C. and Naguib, A. S., "The Prediction of the Fluctuations in the Properties of Free, Round-Jet, Turbulent Diffusion Flame," Combustion and Flame, Vol. 24, pp. 109-124, 1975.

21. Gosman, A. D., Lockwood, F. C. and Syed, S. A., "Prediction of a Horizontal Free Turbulent Diffusion Flame," Sixteenth Symposium (International) on Combustion, The Combustion Institute, Pittsburgh, PA, pp. 1543-1555, 1976.

22. Shearer, A. J., Tamura, H. and Faeth, G. M., "Evaluation of a Locally Homogeneous Flow Model of Spray Evaporation," J. of Energy, Vol. 3, pp. 271-278, 1979.

23. Mao, C. P., Szekely, G. A., Jr. and Faeth, G. M., "Evaluation of a Locally Homogeneous Flow Model of Spray Combustion," J. of Energy, Vol. 4, pp. 78-87, 1980.

24. Ahmad, T. and Faeth, G. M., "Turbulent Wall Fires," Seventeenth Symposium (International) on Combustion, The Combustion Institute, Pittsburgh, PA, pp. 1149-1160, 1979.

25. Markstein, G. H., "Scaling of Radiative Characteristics of Turbulent Diffusion Flames," Sixteenth Symposium (International) on Combustion, The Combustion Institute, Pittsburgh, PA. pp. 1407-1419, 1977.

26. Gordon, S. and McBride, B. J., "Computer Program for Calculation of Complex Chemical Equilibrium Compositions, Rocket Performance, Incident and Reflected Shocks, and Chapman-Jouget Detonations," NASA SP-273, 1971.

27. Mitchell, R. E., Sarofim, A. F. and Clomberg, L. A., "Partial Equilibrium in the Reaction Zone of Methane-Air Diffusion Flames," Combustion and Flame, Vol. 37, pp. 201-206, 1980.

28. Launder, B. E. and Spalding, D. B., Lectures in Mathematical Models of Turbulence, Academic Press, London, 1972.

29. Morton, B. R., "Modeling Fire Plumes," Tenth Symposium (International" on Combustion, The Combustion Institute, Pittsburgh, PA, pp. 973-982, 1965.

30. Magnussen, B. F. and Hjertager, B. H., "On Mathematical Modeling of Turbulent Combustion with Special Emphasis on Soot Formation and Combustion," Sixteenth Symposium (International) on Combustion," The Combustion Institute, Pittsburgh, PA, pp. 719-729.

31. Edwards, D. C., Glassen, L. K., Hauser, W. C. and Tuchscher, J. S., "Radiation Heat Transfer in Nonisothermal Nongray Gases," J. Heat Transfer, Vol. 89, pp. 219-229, 1967.

32. Siegel, R. and Howell, J. R., Thermal Radiation Heat Transfer, McGraw-Hill Book Company, New York, 1972.

33. Fox, P. A., "DESUB: Integration of a First-Order System of Ordinary Differential Equations," Mathematical Software (ed. John R. Rice), Academic Press, New York, 1971.

34. You, H-Z., "An Investigation of Fire Plume Impingement on a Horizontal Ceiling," Ph.D. Thesis, The Pennsylvania State University, University Park, PA, March, 1981.

35. Bilger, R. W., "Probe Measurements in Turbulent Combustion," Progress in Astronautics and Aeronautics, Vol. 53, AIAA, pp. 49-69, 1977.

36. Chen, C. J. and Nikitopoulos, C. P., "On the Near Field Characteristics of Axisymmetric Turbulent Buoyant Jets in a Uniform Environment," Int. J. Heat Mass Transfer, Vol. 22, pp. 245-255, 1979.

37. Ricou, F. P. and Spalding, "Measurements of Entrainment by Axisymmetrical Turbulent Jets," J. Fluid Mech., Vol. 11, pp. 21-32, 1961.

38. Ellison, T. H. and Turner, J. S., "Turbulent Entrainment in Stratified Flows," J. Fluid Mech., Vol. 6, pp. 423-448, 1959.

39. Poreh, M., Tsuei, Y. G. and Cermak, J. E., "Investigation of a Turbulent Radial Wall Jet," J. Applied Mech., Vol. 89, pp. 457-463, 1967.

40. Heskestad, G., "Similarity Relations for the Initial Convective Flow Generated by Fire," ASME Paper No. 72-WA/HT-17, 1972.

NBS-114A (REV. 2-80)

U.S. DEPT. OF COMM. **BIBLIOGRAPHIC DATA SHEET** *(See instructions)*	1. PUBLICATION OR REPORT NO. NBS-GCR-81-304	2. Performing Organ. Report No.	3. Publication Date December 1981

4. TITLE AND SUBTITLE

An Investigation of Fire Impingement on a Horizontal Ceiling

5. AUTHOR(S)

H-Z. You and G.M. Faeth

6. PERFORMING ORGANIZATION *(If joint or other than NBS, see instructions)*

Pennsylvania State University
Department of Mechanical Engineering
University Park, Pennsylvania

7. Contract/Grant No.

Grant 7-9020

8. Type of Report & Period Covered

9. SPONSORING ORGANIZATION NAME AND COMPLETE ADDRESS *(Street, City, State, ZIP)*

U.S. Department of Commerce
National Bureau of Standards
Washington, D.C. 20234

10. SUPPLEMENTARY NOTES

☐ Document describes a computer program; SF-185, FIPS Software Summary, is attached.

11. ABSTRACT *(A 200-word or less factual summary of most significant information. If document includes a significant bibliography or literature survey, mention it here)*

The structure and heat transfer properties of fires and fire plumes impinging on a horizontal ceiling were investigated. Profiles of mean velocity, temperature, composition and mixture fraction were measured. Turbulence quantities were also measured in the plume, including longitudinal fluctuations and Reynolds stress. Other measurements were as follows: convective and radiative heat fluxes to the ceiling, radiative heat flux to the surroundings, and flame shape.

The measurements were compared with predictions of both differential and integral models. A k-ε-g differential model was examined for the plume portion of the flow. This model was originally developed for forced combustirg flows and while it includes buoyancy affects in the mean equations, the effect of buoyancy on turbulence quantities is ignored. The prediction of radiation was simplified, in order to avoid complications due to the presence of soot, by either neglecting radiative heat losses entirely or by assuming that a fixed fraction, 20%, of the energy released by combustion was lost due to radiation.

Integral models were developed for both the plume and ceiling jet portions of the flow. Computational convenience was emphasized during the construction of these models; therefore, "top-hat" profiles a flow entrainment expression, and a mixing-controlled combustion model are assumed.

12. KEY WORDS *(Six to twelve entries; alphabetical order; capitalize only proper names; and separate key words by semicolons)*

ceilings; fire models; fire plumes; heat transfer; radiation; turbulence

13. AVAILABILITY

☒ Unlimited

☐ For Official Distribution. Do Not Release to NTIS

☐ Order From Superintendent of Documents, U.S. Government Printing Office, Washington, D.C. 20402.

☒ Order From National Technical Information Service (NTIS), Springfield, VA. 22161

14. NO. OF PRINTED PAGES

83

15. Price

$9.50

USCOMM-DC 6043-P80